Metric, kilometric and large-scale coherence of metamorphic conditions from graphitic phyllite in the Upper Lesser Himalaya of Nepal: Contribution to the estimation of carbon stored during Himalayan orogeny

Sandeep Thapa, Frédéric Girault, Damien Deldicque, Rémi Losno, Christian France-Lanord, Chiara Groppo, Franco Rolfo, Shashi Tamang, Thomas Rigaudier, Baptiste Debret, et al.

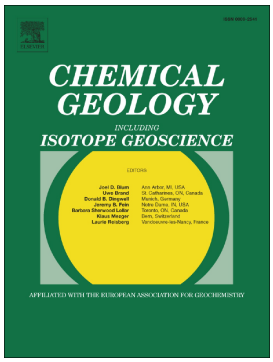

Metric, kilometric and large-scale coherence of metamorphic conditions from graphitic phyllite in the Upper Lesser Himalaya of Nepal: Contribution to the estimation of carbon stored during Himalayan orogeny

Sandeep Thapa, Frédéric Girault, Damien Deldicque, Rémi Losno, Christian France-Lanord, Chiara Groppo, Franco Rolfo, Shashi Tamang, Thomas Rigaudier, Baptiste Debret, Kabi Raj Paudyal, Lok Bijaya Adhikari, Frédéric Perrier

PII: S0009-2541(23)00078-5

DOI: https://doi.org/10.1016/j.chemgeo.2023.121378

Reference: CHEMGE 121378

To appear in: *Chemical Geology*

Received date: 27 March 2022

Revised date: 6 February 2023

Accepted date: 8 February 2023

Please cite this article as: S. Thapa, F. Girault, D. Deldicque, et al., Metric, kilometric and large-scale coherence of metamorphic conditions from graphitic phyllite in the Upper Lesser Himalaya of Nepal: Contribution to the estimation of carbon stored during Himalayan orogeny, *Chemical Geology* (2023), https://doi.org/10.1016/j.chemgeo.2023.121378

Metric, kilometric and large-scale coherence of metamorphic conditions from graphitic phyllite in the Upper Lesser Himalaya of Nepal: Contribution to the estimation of carbon stored during Himalayan orogeny

Sandeep Thapa[1*], Frédéric Girault[1], Damien Deldicque[2], Rémi Losno[1], Christian France-Lanord[3], Chiara Groppo[4,5], Franco Rolfo[4,5], Shashi Tamang[1,4], Thomas Rigaudier[3], Baptiste Debret[1], Kabi Raj Paudyal[6], Lok Bijaya Adhikari[7], and Frédéric Perrier[1]

[1]Université Paris Cité, Institut de Physique du Globe de Paris, CNRS, F-75005 Paris, France

[2]Laboratoire de Géologie, École Normale Supérieure/CNRS UMR 8538, PSL Research University, F-75005 Paris, France

[3]Centre de Recherches Pétrographiques et Géochimiques, Université de Nancy, CNRS, F-54500 Vandoeuvre-lès-Nancy, France

[4]Department of Earth Sciences, University of Torino, via Valperga Caluso 35, 10125 Torino, Italy

[5]CNR-IGG, via Valperga Caluso 35, 10125 Torino, Italy

[6]Central Department of Geology, Tribhuvan University, Kathmandu, Nepal

[7]Department of Mines and Geology, National Seismological Centre, Lainchaur, Kathmandu, Nepal

[*]Corresponding author. Email address: thapa@ipgp.fr (S. Thapa)

February 2023, revised version submitted to *Chemical Geology*

Abstract

Besides carbonates, carbonaceous material in meta-sediments represents an important carbon reservoir on Earth. In orogenic belts, carbon can be stored as graphite, a contribution to the global carbon cycle that remains insufficiently constrained. Here, we focus on the Himalayan belt where moderately crystalline graphite is found at the footwall of the Main Central Thrust. Using various analytical methods, we investigate metamorphic conditions of graphite at increasing spatial scales in the Upper Lesser Himalayan Sequence (upper-LHS) phyllites of Nepal. First, we develop and validate a new SEM-BSE technique to measure total organic carbon (TOC) content. Graphite shows mostly inter- and intra-granular flaky crystals associated with carbonates. Elemental carbon analyses yield large range of TOC content in phyllites with a mean of 3.7±0.4 vol.%. Inferred from micro-Raman spectroscopy, peak metamorphic temperature (peak-*T*) ranges from 519±9 to 590±8 °C. We observe a significant coherence of metamorphic conditions of graphitic phyllites at metric, decametric and kilometric scales using extensive data obtained in the Upper Trisuli valley, Central Nepal (*n*=77), and, at larger spatial scales, using data from Far-Western to Eastern Nepal (*n*=67). Mean carbon isotopic composition ($\delta^{13}C$) of −26.3±0.1 ‰ indicates biogenic source. Less negative $\delta^{13}C$ values, also reported in other orogenic belts, suggest interaction with pre-existing sedimentary carbonates, probably related to metamorphic isotopic re-equilibration. First-order extrapolations at the upper-LHS scale suggest meta-sediment organic carbon may represent up to 20 % of the total amount of carbon stored in orogens. Central Nepal segment, with higher TOC content and peak-*T*, is also characterized by the largest current metamorphic carbon dioxide (CO_2) emissions of the chain. This hardly coincidental association, at the scale of the Himalayan belt, between organic carbon stored as graphite and mobile inorganic carbon released as CO_2 represents an important clue to investigate further for global carbon budget estimations.

Abstract word count: 296 (≤ 300 words)

Manuscript word count: 11609

Keywords: Main Central Thrust; Graphite; Carbonaceous material; Raman spectroscopy; Scanning Electron Microscopy; Carbon budget

1. Introduction

Elemental carbon is ubiquitous on the Earth's surface and at depth due to the large stability field of its polymorphs (Hayes and Waldbauer, 2006; Beyssac and Rumble, 2014). In metamorphic rocks, the recrystallization of carbonaceous material starts from 350–430 °C (Grew, 1974; Wang, 1989; Nakamura et al., 2020) and, depending on pressure, well-ordered graphite crystals form at around 600–700 °C (Henry et al., 2019; Nakamura et al., 2020). Regional and contact metamorphism, deformation or fluids contribute to graphite genesis whose crystallinity increases with increasing metamorphic grade (Miyashiro, 1964; Itaya, 1981; Wang, 1989; Pasteris and Wopenka, 1991; Wada et al., 1994; Beyssac et al., 2003; Kříbek et al., 2008; Aoya et al., 2010; Skrzypek, 2021). In most cases, organic matter is the precursory material originally present in the sedimentary protolith rock from which graphite crystallizes at greenschist to granulite facies conditions (Landis, 1971; Diessel et al., 1978; Buseck and Huang, 1985; Beyssac et al., 2016; Kirilova et al., 2018). Throughout graphitization, pressure impacts the physical changes while temperature is responsible for the chemical transformation (Buseck and Beyssac, 2014). During subduction, graphitic-like carbon may be consumed through oxidation or dissolution in fluids, or can be preserved and later exhumed (Galvez et al., 2013; Bouilhol et al., 2022). Graphitic-like carbon can also have inorganic origin, when deposited from COH fluids or formed through complex redox reactions (*e.g.*, Connolly and Cesare, 1993; Satish-Kumar et al., 2002, 2011; Groppo et al., 2013; Craw and Upton, 2014; Debret et al., 2022). Graphite is indeed observed in active shear zones worldwide (Mathez et al., 1995; Craw and Upton, 2014; Parnell and Brolly, 2021). Thrust faults impact the chemical upgrade of the carbon in the fault zone due to frictional effect (Nover et al., 2005; Nakamura et al., 2015; Muirhead et al., 2021). Active faults may also modify the previously stored carbonaceous material or promote the formation of new carbonaceous material (*e.g.*, Oohashi et al., 2014; Hirono et al., 2015; Kirilova et al., 2018; Nakamura et al., 2018). In collisional orogenic settings, where metamorphism, deformation

and fluids have been active for a longer duration, graphite-rich rocks are widespread and represent important carbon reservoirs (*e.g.*, Parnell et al., 2021; Parnell and Brolly, 2021; Müller et al., 2022). Besides carbonates and calcsilicate rocks, which have been shown to significantly contribute to the CO_2 production through decarbonation reactions (*e.g.*, Ague, 2000; Groppo et al., 2013, 2022; Rapa et al., 2017), it appears therefore important to better constrain the properties and the quantity of organic carbon stored as graphite in orogenic belts. A precise knowledge of the total amount of carbon stored within these rocks, as well as of the genetic mechanisms involved in their formation, is indeed crucial for our understanding of the processes controlling carbon storage, transfer and release in the Earth's crust (*e.g.*, Kelemen and Manning, 2015; Plank and Manning, 2019).

Precambrian rocks rich in organic carbon are widely exposed in the Himalaya (Stöcklin, 1980), the largest active orogenic belt on Earth. Their occurrences at mid-crustal depth is also suggested by the mid-crustal high electrical conductivity anomalies, which have been variably interpreted as due to the presence of fluids, brines or conductive layers such as graphitic rocks (*e.g.*, Lemonnier et al., 1999; Unsworth et al., 2005; Arora et al., 2007; Börner et al., 2018; Groppo et al., 2022). Graphitic phyllites, containing amorphous carbon and moderately to well crystalline graphite, form a more or less continuous unit in the Upper Lesser Himalayan Sequence (upper-LHS), located few hundreds of meters below the Main Central Thrust (MCT) (*e.g.*, Ishida, 1969; Arita et al., 1984; Goscombe et al., 2006; Webb et al., 2007; Kohn, 2008; Jessup et al., 2008; Paudel, 2011; Larson, 2012; Yakymchuk and Godin, 2012; From and Larson, 2014; Wang et al., 2015; Shrestha et al., 2017). Preliminary estimates of the total amount of carbon stored in such graphitic phyllites are scarce (*e.g.*, Evans et al., 2008; Paudel, 2011; Rana et al., 2021). Their carbon isotopic composition ($\delta^{13}C$) mainly shows organic origin, but significant discrepancies exist probably caused by enrichment in ^{13}C during interaction with carbonates (Evans et al., 2008; Sharma et al., 2011, Rana et al., 2021; Kiran et al., 2022). To determine the thermal maturity of organic carbon (Henry et al., 2019), micro-Raman spectroscopy of carbonaceous material (RSCM) has been applied on these graphitic phyllites along

different cross-sections in the LHS, confirming the existence of an inverted temperature gradient below the MCT (Beyssac et al., 2004; Bollinger et al., 2004). Thus, the available previous studies demonstrated that graphitic phyllites systematically recorded the highest peak metamorphic temperatures within the LHS, with values ranging from about 550 to 620 °C (Beyssac et al., 2004; Bollinger et al., 2004; Rawat and Sharma, 2011; Mathew et al., 2013; Long et al., 2016; Rana et al., 2021). However, before attempting large-scale estimates, it is important to evaluate whether these results are punctual or can be taken as sufficiently representative. In addition, in the vicinity of the upper-LHS graphitic phyllites, carbon dioxide (CO_2) emissions of metamorphic origin have been reported (*e.g.*, Becker et al., 2008; Evans et al., 2008; Girault et al., 2014, 2018, 2022, in press a,b). The simultaneous presence of stored carbon (carbonates and graphite) and released carbon (CO_2 emissions) at a large spatial scale raises the question as to whether these processes are related and what might be the contribution of graphitic phyllite to the carbon stored during Himalayan orogeny.

In this paper, to address the limitations stated above, we focus on the upper-LHS graphitic phyllites. First, we develop a new technique based on Scanning Electron Microscope and Back-Scattered Electron (SEM-BSE) images to estimate organic carbon (graphite) content directly from thin sections. Second, we study in details five sites located in the Upper Trisuli valley, Central Nepal, a few hundreds of meters south of the MCT. After describing the graphite characteristics, the metamorphic conditions from graphitic phyllites are studied using various analytical methods at increasing spatial scales. Carbon isotopic composition of graphitic phyllites is also studied in relation with total, organic and inorganic carbon content. Based on our additional data from Far-Western to Eastern Nepal, and complemented by published data from other workers, we discuss the possible connection between occurrences of graphite and locations of current CO_2 emissions, and the implications of our results on stored carbon for the carbon budget in the Himalaya and in other orogenic belts.

2. Geological background and samples

2.1 Geological setting

Resulting from the collision of the Indian plate and the Eurasian plate which started 60–40 Ma ago, the Himalaya is the largest active orogenic belt on Earth (Le Fort, 1975). The Nepal Himalaya shows various tectonostratigraphic units separated by several thrust and fault systems (Fig. 1a). Related at depth to the Main Himalayan Thrust (MHT) which accommodates the convergence (*e.g.*, Avouac, 2003), the Main Central Thrust (MCT) separates low- to medium-grade metamorphic rocks of the Lesser Himalayan Sequence (LHS) to the south from the higher-grade metamorphic rocks of the Greater Himalayan Sequence (GHS) to the north (Upreti, 1999; Searle et al., 2008). Consisting of a 10-to-15-km-thick sequence of unmetamorphosed sedimentary units to greenschist-grade metasedimentary units, LHS rocks started deposition about 1880 Ma (*e.g.*, Kohn et al., 2010). They also show an inverted metamorphic series from lower greenschist-grade to the south (*P-T* conditions: 8 kbar and 340 °C) up to garnet-bearing isograds beneath the MCT (*P-T* conditions: 9.5–12 kbar and 590 °C) (Arita, 1983; Beyssac et al., 2004; Khanal et al., 2020; Wang et al., 2022; Tamang et al., 2023). GHS rocks are younger about 1100 to 440 Ma (*e.g.*, Parrish and Hodges, 1996). Within the MCT shear zone, the Ramgarh Thrust (RT), located southward MCT, separates the oldest LHS rocks from the younger LHS rocks (Pearson and DeCelles, 2005).

This study focusses on graphitic phyllites from the upper-LHS located in the MCT zone of the Nepal Himalaya. The Upper Trisuli valley (Fig. 1b), located about 60 km north of Kathmandu in Central Nepal and crossed by Bhote Koshi, Langtang and Chilime Rivers, exhibits a representative graphitic mica-schist unit between the MCT and RT. Along this transect, GHS rocks encompass, from south to north, the kyanite schist and gneiss unit which includes medium to coarse grained kyanite-gneiss and garnet schist, the quartzite unit which includes fine to medium grained quartz with garnet,

and the banded and migmatitic gneiss unit consisting of feldspar, quartz, muscovite, biotite, garnet and tourmaline (Tagaki et al., 2003; Dhital, 2015; Khanal et al., 2020). LHS rocks encompass, from south to north, the garnet schist unit with garnet schist, meta-sandstone and sericitic phyllite also named as "Kuncha formation" (Stöcklin, 1980; Kohn et al., 2005; Girault et al., 2012), the graphitic mica-schist unit which overlies the garnet schist unit and consists of carbonate bands, fine to medium grained garnet schist and graphitic phyllite (Kohn, 2008; Dhital, 2015), and the overlying augen gneiss unit which includes Ulleri-type medium to coarse grained orthogneiss (Kohn et al., 2005, 2010; Dhital, 2015).

In the Upper Trisuli valley (Fig. 1b), the graphitic mica-schist unit is well-exposed in the Chilime tributary valley along the road sections of Pajung village and Paragaon village (well-known as Tatopani), and of Tetangchet village nearby the upper Sanjen hydropower site. Mineralogically, the graphitic phyllites mainly consist of quartz (42±12 %), phlogopite (16±3 %), muscovite (12±2 %), graphite (6±1 %) and pyrite (4±1 %) (Börner et al., 2018). Aluminum-rich minerals such as garnet and staurolite are reported in graphitic phyllites in the same valley (Kohn, 2008; Goscombe et al., 2018; Rapa et al., 2018; Tamang et al., 2023). Finally, several occurrences of pluridecimetric bands of carbonates (siliceous dolomitic marble) are also observed within the unit.

2.2 Description of the outcrops

Within the graphitic mica-schist unit, several outcrops oriented west-east expose the metamorphic rocks along the Chilime River and along the roads from the Bhote Koshi-Chilime confluence to the Paragaon village and to the upper Sanjen hydropower site. Five sites were investigated in January 2020 and January-February 2021 (Fig. 1b): a 400-m-long outcrop located upward Pajung village (site A; Fig. 1c), a 100-m-long outcrop located downward Pajung village (site B; Fig. 1d), a 50-m-long outcrop located near Goljung village (site C; Fig. 1e), a 125-m-long outcrop

located near Sanjen hydropower site (site D; Fig. 1f) and a 90-m-long outcrop located downward Paragaon village (site E; Fig. 1g). At the five sites, fresh and unweathered rock samples were collected, benefitting from fresh scarps made by road construction. For each sample, about 150 g of rock was crushed in powder manually in the field without sieving and placed in a plastic bag, and one to five small representative pieces of 5 cm size maximum were also collected. A total of 77 graphitic phyllite samples were collected with 5 to 10 m spacing in between two samples depending on the considered site: 43 samples at site A (A1-A43) including 25 samples at higher resolution with a sampling interval of 1 m plus one sample of a preliminary survey (ME1), 6 samples at site B (B1-B6), 7 samples at site C (C1-C7), 8 samples at site D (D1-D8) plus two samples of a preliminary survey (ME9 and ME15), and 10 samples at site E (E1-E10). Sampling was done with the utmost caution not to collect samples in the same layer, hence avoiding sampling redundancy. This sampling strategy allows us to study the heterogeneity of the graphitic mica-schist unit of the Upper Trisuli valley at various spatial scales, from meter-scale to formation scale.

To compare with other valleys in Nepal in similar geological contexts, a total of 67 additional graphitic phyllite samples collected during other campaigns in other locations of Nepal were also used. In Far-Western Nepal, we collected: 2 samples from Dharchula area near Khotila and above Pasti in June 2022, 4 samples from Mugu-Karnali valley near Gamgadhi in November 2018 and 5 samples from Humla-Karnali valley along the Jumla-Simikot way in October 2021. In mid-Western Nepal, we collected 4 samples in Lower Dolpo above Rupagad and Tarakot from 2009 to 2011. In Western Nepal, we collected: 10 samples in Kali Gandaki valley near Narchyeng in December 2020 (Supp. Fig. S1), 3 samples in Marsyangdi valley near Ngadi in April 2018 and 2 samples near Barpak in May 2016. In Central Nepal, we collected: 2 samples in Ankhu valley (“Ruby valley”) near Lapa in 2017, and 1, 3 and 13 samples in Bhote Koshi valley near Kodari in August 2009, December 2020 (Supp. Fig. S2) and April 2021, respectively. In Eastern Nepal, we collected: 8 samples in Leuti area (Supp. Fig. S3) and 8 samples in Akhuwatar area (Supp. Fig. S4) in December 2020, and 2 samples

in Chainpur area in October 2021. A complete list of all the studied samples together with their location is available as Supp. Table S1.

3. Sample analysis

To study the graphitic phyllite samples, we focused on the determination of the organic, inorganic and total carbon contents and on the characterization of the graphite using different analytical techniques. The methods described below also include the presentation and validation of a new approach based on scanning electron microscopy to estimate graphite content in rock samples.

In the following, every uncertainty associated with a parameter for a sample is given at one-sigma (68 % confidence level). The uncertainty of an average value of a parameter calculated for a given group of samples corresponds to the standard error, *i.e.* the standard deviation divided by the square root of the number of data. All average values are arithmetic means, except stated otherwise.

3.1 Analytical methods

3.1.1 Petrography and graphite morphology

Representative samples of graphitic phyllite were selected to study the mineral assemblages: some with an abundant graphite content and others with less graphite associated with carbonate minerals. Thin sections were prepared after induration of the samples. They were studied at University of Turin, Italy under an Olympus BX4 reflected and transmitted polarized light microscope. Photomicrographs were taken with an attached JENOPTIK ProgResC5 digital color camera. Two samples were studied in detail under a Scanning Electron Microscope (SEM) at École Normale Supérieure (ENS), Paris, France to analyze their mineralogical composition. In addition,

several high-resolution SEM photomicrographs were taken to study the morphology of the graphite minerals.

3.1.2 Micro-Raman spectroscopy on carbonaceous material

3.1.2.1 Principle and sample preparation

The Raman spectrum of carbonaceous material (RSCM) consists of a two-order spectrum depending on the degree of crystallization: the first-order region in the wavelength range of 1100–1800 cm^{-1} and the second-order region in the range of 2500–3100 cm^{-1} (Tuinstra and Koenig, 1970). Here, we recorded data over the 700–2100 cm^{-1} range, hence including the first-order region in totality, which depends on the different *P-T* conditions. All the studied Raman spectra include the three D1, G and D2 bands. The graphite band (G), whose position is between 1580 and 1600 cm^{-1}, corresponds to in-plane vibration of aromatic carbons. The other bands (mainly D1 and D2) correspond to in-plane defects in the carbon structure. These D1 and D2 bands, occurring respectively at 1350 and 1620 cm^{-1}, are large and intense in poorly ordered carbonaceous material and decrease in both width and intensity when the crystallinity of graphite increases (Rouzaud et al., 1983).

To characterize graphite in the phyllite samples, a non-polished millimeter size sample was prepared. Raman spectra were acquired especially on fresh samples with the help of a confocal Raman microscope (inVia™, Renishaw, UK) coupled with an optical microscope (Leica, Germany) at ENS, Paris, France. The microscope allowed focusing the excitation laser beam on the sample at 514.5 nm, due to the dispersive behavior of the defect bands, in order to collect Raman signal. It was equipped with a Kensington controller and adjustment was made with 50x magnification objective lens for proper visualization. The Raman scattered light was dispersed using 100 lines per mm grating and detected by a CDD camera (Philips SPC 900NCPC camera). The laser power on the sample was

maintained lower than 0.2 mW to avoid sample heating. A single acquisition lasted 20 s. Five acquisitions were performed to obtain one spectrum, reducing fluorescence effect (*i.e.* non-horizontal spectrum; some remain and are shown in Fig. 2a). As the samples appeared relatively homogeneous, stacking only 10 spectra per sample was found sufficient to reduce the standard deviation and thus obtain a representative final spectrum of each sample. This procedure follows common sample preparation details (*e.g.*, Beyssac et al., 2002; Aoya et al., 2010; Nakamura and Akai, 2013; Kouketsu et al., 2014).

As an example, Fig. 2 shows the ten Raman spectra obtained from sample A28. All the three bands are clearly visible and show some variations between the spectra depending on the considered target (Fig. 2a). After baseline correction, the maxima of each band can be compared (Fig. 2b). Then, the D1, G and D2 bands of each spectrum were analyzed in terms of peak position of band area, band intensity or height and band surface area, as depicted in Fig. 2c, with conventional fitting procedures based on a Voigt function using PeakFit® software (Systat Software, Inc., USA) (Lünsdorf et al., 2013). The peak positions of the D1, G and D2 bands from all outcrops remain relatively similar and range from 1356.1±0.5 to 1357.9±0.3 cm^{-1} (mean: 1357.0±0.3 cm^{-1}), from 1578.9±0.5 to 1581.1±0.1 cm^{-1} (mean: 1579.9±0.4 cm^{-1}) and from 1617.2±0.2 to 1620.7±0.3 cm^{-1} (mean: 1619.3±0.6 cm^{-1}), respectively. We also determined the full widths at half maximum (FWHM) for each band. The D1-, G- and D2-FWHM are related to the maturity of the rocks (Kouketsu et al., 2014; Henry et al., 2019). On average, relative uncertainty for the values of D1-, G- and D2-FWHM were 4.1±0.3 %, 3.3±0.9 % and 16±1 %, respectively. On average, for a given sample, the mean dispersion of the values obtained from the ten spectra was 2.78±0.01 %.

3.1.2.2 Determination of peak metamorphic temperature

Using the RSCM data, we estimated the peak metamorphic temperature (peak-*T*) attained by the considered sample. For this purpose, we compared the three well-established different geo-thermometer relationships. The Beyssac et al. (2002) geo-thermometer is based on temperature conditions reached during regional metamorphism and on the following linear empirical relationship:

$$T(°C) = 445R2 + 641 \quad , \tag{2}$$

where

$$R2 = \left(\frac{\mathrm{D1}}{\mathrm{G} + \mathrm{D1} + \mathrm{D2}}\right)_{\mathrm{A}} \quad , \tag{3}$$

where the subscript A refers to the surface area of the D1, G and D2 bands. Eq. (2) is applicable for all types of organic precursor, relevant in the temperature range 330–650 °C, and was applied with success to Himalayan metamorphic rocks (Beyssac et al., 2003, 2004; Bollinger et al., 2004).

To overcome the effects of metamorphic pressure from the lower and higher-temperature rocks, a modified RSCM thermometer based on the *R*1 and *R*2 ratios was introduced, with the following empirical equation (Rahl et al., 2005):

$$T(°C) = 737.3 + 320.9\,R1 - 1067\,R2 - 80.638\,(R1)^2 \,, \tag{4}$$

where

$$R1 = \left(\frac{\mathrm{D1}}{\mathrm{G}}\right)_{\mathrm{H}} \,, \tag{5}$$

where the subscript H refers to the height or intensity of the D1, G and D2 bands. The reliability of this thermometer extends to the temperature range 100–700 °C.

More recently, Aoya et al. (2010) compared the orientation of the materials with the laser beams parallel and normal to the *c*-axis and concluded that the results are comparable within the *R*2 ratios. Here, we used the following quadratic empirical equation for regional metamorphism which is valid for the temperature range 340–650 °C (Aoya et al., 2010):

$$T(°C) = 91.4\,(R2)^2 - 556.3\,(R2) + 676.3 \quad . \tag{6}$$

The peak-*T* of a total of 74 samples was determined by RSCM using the three geo-thermometers. They are written hereinafter B-, R- and A-RSCM for Beyssac et al. (2002), Rahl et al. (2005) and Aoya et al. (2010) method, respectively. For each sample, we used the average values of the parameters determined above based on the ten recorded Raman spectra studied per sample. Absolute uncertainty on the determination of peak-*T* remained generally small and ranged from 1.6 to 19 °C for B-RSCM, from 2.0 to 16 °C for R-RSCM and from 2.5 to 22 °C for A-RSCM.

For a given sample, R-RSCM and A-RSCM geo-thermometers show higher peak-*T* values than the ones obtained using the B-RSCM geo-thermometer. When considering all our samples, the difference in peak-*T* appears to be linear in the B-RSCM temperature range 518.7–589.9 °C (Supp. Fig. S5). On average, B-RSCM peak-*T* is 9.1±0.2 % lower than A-RSCM peak-*T* and 9.7±0.2 % lower than R-RSCM peak-*T*. R-RSCM peak-*T* is lower and higher than A-RSCM peak-*T* in the range 520–560 °C and 560–650 °C, respectively. While the difference between A-RSCM and B-RSCM methods seems to show a simple shift, the differences with R-RSCM appear more complicated (Supp. Fig. S5). These systematic differences are important to be considered when working on metamorphic rocks. The A-RSCM peak-*T* calculation depends on the intensity of bands (*R*1), that of the B-RSCM on the area of bands (*R*2) and that of the R-RSCM on both parameters, which may explain the more complicated behavior of R-RSCM compared with the two other methods (Mathew et al., 2013). In addition, B-RSCM mainly considers that the crystallinity of carbonaceous material depends on metamorphic temperature, while R-RSCM takes into account both metamorphic pressure and temperature. Comparing these peak-*T* data with other estimated peak metamorphic temperature inferred from thermodynamic modelling on similar graphitic phyllite samples of the same lithostratigraphic unit (Tamang et al., 2023) suggests that A-RSCM and R-RSCM methods overestimate the peak-*T* values while the B-RSCM method tends to give more consistent peak-*T* values. This tentative explanation remains preliminary at this stage and motivates further benchmark

exercises to compare directly the different approaches estimating a peak metamorphic temperature of a given sample. In the following, B-RSCM peak-*T* calculation is thus used.

We compared for the same samples the calculations of *R*1 and *R*2 parameters and peak-*T* done by the same operator using two different softwares: PeakFit® (Systat Software, Inc., USA) and WiRE (Renishaw, UK). With a total of 11 samples, in the B-RSCM temperature range 530–590 °C, the use of PeakFit® or WiRE software does not show any clear difference (Supp. Fig. S6). Indeed, the mean difference is 6±1 %, hence within the overall experimental uncertainty of the method. In addition, the particular software used does not introduce additional differences (Supp. Fig. S7). In the following, the PeakFit® software is used for the determination of peak-T.

3.1.3 Carbon contents using an elemental analyzer

For each sample, about 70 to 80 g of rock chunks were grounded. For total carbon (TC) content, an amount of about 8 mg was weighted with a microbalance and wrapped in a tin capsule for analysis. For total organic carbon (TOC) content, we used the rinsing method which consists in the decarbonation of the sample using hydrochloric acid to remove the inorganic carbon (IC) from TC content of the sample (Koni zer et. al., 2012; Fujisaki et al., 2021). This decarbonation method does not affect the carbon isotopic composition (Midwood and Boutton, 1998; Schubert and Nielsen, 2000). Approximately 4 to 6 g of powdered sample was placed into a beaker where 100 mL of 1.5 mol L^{-1} HCl solution was poured. After 24 h, the solution was diluted by adding 400 mL of distilled water. Again after 24 h, the sample was rinsed two times with distilled water with extra care not to lose some sample powder. Then, the sample was kept for drying to evaporate the remaining water in the beaker. Finally, the dried sample was grounded and weighted to about 8 mg into tin capsules for analysis.

The prepared samples were analyzed for TC and TOC using a Flash 2000 organic CHNS Elemental Analyzer (Thermo Scientific™, USA) at Institut de Physique du Globe de Paris (IPGP), France. The tin capsule containing the sample was introduced into the combustion reactor with oxygen and the resulted gases were facilitated by the helium flow (used as carrier gas) which was swept through a gas chromatography (GC) column. Then, combustion gases were separated by a GC column and detected by a thermal conductivity detector. CHNS calibration was performed using Aspartic Acid having the technical specification of 36 C%. The calibration factor remained relatively stable with a dispersion of about 2 % (n=13) throughout the measurement sequences.

We measured TC content on samples powdered in the field and on cm-size pieces crushed in the laboratory. The dispersion of TC content on pieces of the same sample was considered too large and we retained only the values obtained on the powdered samples. In this paper, we determined TC and TOC contents, as a mass ratio expressed in wt %, of a total of 77 graphitic phyllite samples from the Upper Trisuli valley and 67 graphitic phyllite samples from other locations in Nepal. Relative experimental uncertainty on the carbon mass ratio, inferred from systematic tests, ranged from 0.5 to 11 % for TC content and from 1.4 to 5.4 % for TOC content. For each sample, IC was inferred by subtracting the TOC content value to the TC content value. Mean relative uncertainty for IC was 29±6 %.

The repeatability of the measurement of carbon content was evaluated independently using repeated measurements of the Aspartic Acid solution. It gave a dispersion of about 2 %, moderately compatible with the value given by the manufacturer (1 %). Four powdered samples were replicated multiple times to estimate the carbon content dispersion within the sample. Relative difference of graphitic phyllite replicates ranged from 1.4 to 5.4 %, with a mean of 4.3±1.0 %. From measurements repeated 3 to 4 times, we obtained a satisfactory repeatability of the results, with a coefficient of variation for a single measurement smaller than 3 % in most cases. A total of 20 powdered samples were also analyzed by the Thermo Scientific elemental analyzer IsoLink IRMS System at Centre de

Recherches Pétrographiques et Géochimiques (CRPG), Nancy, France. To calculate carbon concentration, the thermal conductivity detector signals were calibrated with internal standards: BFSd (C=0.53 wt.%), CRPG_M2 (C=0.408 wt.%), Eurovector Synthetic Soil Mix #4 (C=2.417 wt.%), and Eurovector Synthetic Soil Mix #1 (C=3.5 wt.%). Relative uncertainty was better than 5 %. Relative difference with the results obtained at IPGP (Paris, France) ranged from 0.1 to 15 % with a mean of 7±2 %. This blind comparison gave remarkable consistency between the data obtained with the analyzer used at IPGP and those obtained with another analyzer used at CRPG (Supp. Fig. S8). As we had both the effects of sample dispersion (assessed above to be about 2 to 3 %) and absolute uncertainty, we considered a conservative absolute uncertainty of each instrument of 5 %. To compare with the following new method, the experimental uncertainty was added in quadrature with the absolute uncertainty of 5 %.

3.1.4 Organic carbon content using the new SEM-BSE technique

As a new approach to determine TOC content from graphitic phyllite samples, we used a Scanning Electron Microscope (SEM) coupled with the detection of Back-Scattered Electrons (BSE) and Secondary Electrons (SE). First, a cm-size sample, cut perpendicular to the foliation and parallel to the lineation was prepared in order to fit inside a cylindrical mold. This mold containing the sample was then filled in with resin and epoxy (Supp. Fig. S9a,b). Second, the cylindrical mold containing the sample was incised and polished manually with different grades of polishing paste. Diamond resin polishing discs were used on hand-held machinery maintaining a suitable range of rotations per minute for smoothing the surface. Polishing was first done by 50 µm diamond smoothing disc and followed in decreasing size order by 30, 10, 8 and 5 µm discs (Supp. Fig. S9c). Then, using the two-diamond paste having 1 µm and 0.25 µm sizes, polishing was done manually and carefully on the diamond disc not to lose the soft particles (Supp. Fig. S9d). Finally, the surface of the samples was

coated with gold to make the final sample conductive. The thickness of the coating was maintained to 1–10 nm.

SEM images of 3.4 × 2.3 mm^2 surface area were obtained using a Zeiss Sigma SEM model (Carl Zeiss Microscopy, Germany) at ENS, Paris, France (Fig. 3a,d), with working conditions of 15 kV and distance of ~9 mm. All the images were captured using BSE detector along with a 120 µm diaphragm aperture size. This allowed us to highlight location of elements such as carbon at the surface (Fig. 3b,e). From the obtained SEM image coupled with BSE, the surface area occupied by carbon element was calculated using ImageJ software (National Institutes of Health, USA) on high-resolution SEM images. There are different thresholding methods where multiple of colors help in interpreting the results. Manually, the threshold was checked to overcome the over-estimation of the binary image outputs, as shown in Fig. 3c,f. We used blue color threshold as a background, which represents the black or dark areas from the original image, to quantify the surface area. The specific darker color of graphite allowed us to directly discriminate graphite and carbonate (light grey color), as also shown in Fig. 4c,d. We took the utmost caution to avoid micro-scale cracks in the image that may create artifacts during the thresholding step.

The minimum number of SEM images needed to obtain reliable carbon content values was tested. Using two samples with 20 images and all the other samples with 10 images, we found that both a good stability of carbon content values and an acceptable relative uncertainty on carbon content are reached when more than 5 to 7 images are used (Supp. Fig. S10). In addition, we found that 10 different images, selected by order of their acquisition, gave a sufficient representative value of the whole surface area (about 35 % of the whole sample surface studied). Thus, for each sample, 10 images were captured at different locations and the values of elemental carbon (*i.e.* TOC or graphite in our case) content, expressed in vol.%, were averaged to obtain the mean value and associated uncertainty. An example of 10 images obtained from a single thin-section is shown in Supp. Fig. S11. We obtained in this case a mean TOC content (volumetric ratio) of 4.2±0.4 %, with a dispersion of

values of 32±7 %. In total, we measured the TOC content from a total of 15 samples: eight from site A, two from site C, three from site D and one each from sites B and E. The relative uncertainty ranged from 0.5 to 19.0 %, with a mean of 8±2 %.

3.1.5 Carbon isotopic composition ($\delta^{13}C$)

Determination of stable carbon isotopic composition ($\delta^{13}C$) of the samples was performed on-line using the Thermo Scientific EA IsoLink IRMS System at CRPG Nancy, France. Samples were wrapped in tin capsules (approx. 3 mg) and then combusted by flash pyrolysis (≈1400 °C) in a combustion reactor consisting of quartz tube filled with chromium oxide, pure copper and silvered cobalt oxide. Produced gases (N_2, CO_2 and SO_2) were separated on a GC column maintained at 70 °C and carbon isotopic composition of the produced CO_2 was then measured with a Thermo Scientific Delta V Advantage continuous flow isotope ratio mass spectrometer. Carbon isotopic composition was determined by comparison with two internal and three international standards routinely included during the analysis: BFSd ($\delta^{13}C$=–21.5 ‰), CRPG_M2 ($\delta^{13}C$=–24.98 ‰), NBS22 ($\delta^{13}C$=–30.03 ‰), IAEA CH6 ($\delta^{13}C$=–10.449 ‰) and USGS24 ($\delta^{13}C$=–16.1 ‰). Values are quoted in the delta notation in ‰ relative to V-PDB (Vienna Pee Dee Belemnite) and the reproducibility gives an absolute average value of 0.15±0.09 ‰ (*n*=6). Absolute uncertainty was better than 0.3 ‰. From the five sites in the Upper Trisuli valley, a total of 20 representative graphitic phyllite samples were analyzed for $\delta^{13}C$ from the bulk (non decarbonated or TC). $\delta^{13}C$ from some decarbonated samples (or TOC) were also performed, as well as one dolomite sample. Carbonates, reduced organic matter and mantle derived carbon have mean $\delta^{13}C$ values of about 0 ‰, –25 ‰ and –7 ‰, respectively (Dobner et al., 1978).

3.2 Results of sample analysis

3.2.1 Location, description and morphology of graphite

The studied graphitic phyllite samples belong to the graphitic mica-schist unit which can be classified as high-potassium-aluminum metapelites (Fig. 4 and Supp. Fig. S12). Two samples from site A (A1 and A8) and two samples from site C (C4 and C6) were studied.

Sample A1 (Fig. 4a,c) is a fine-grained graphitic phlogopite-bearing phyllite alternated with calcschist, consisting of quartz, carbonates (both calcite and dolomite), phlogopite, abundant graphite, rare kyanite and accessory apatite. It shows a banded structure, characterized by millimetre-thick carbonate-free, quartz-rich layers alternated with carbonate-bearing layers of similar thickness (Fig. 4a). The main schistosity is defined by phlogopite, which occurs in oriented flakes showing a weak pleochroism from colourless to pale orange (Fig. 4c). Kyanite here is rare and limited to the carbonate-free layers; it forms sub-millimetric porphyroblasts partially replaced by late white mica at the rim. Graphite is equally distributed between the two types of layers and it occurs both as inter-granular and intra-granular phases (*e.g.*, included in quartz and calcite) (Fig. 4c).

Sample A8 (Fig. 4b,d) is a fine-grained graphitic phyllite consisting of quartz, muscovite, phlogopite, abundant graphite and accessory rutile. The pervasive foliation is defined by muscovite and phlogopite, the last being characterized by a weak pleochroism from colourless to pale orange (Fig. 4b). Phlogopite is, on average, less abundant and finer grained than muscovite (Fig. 4d). Graphite is mostly concentrated in fine-grained aggregates of length up to 100 μm, localized at grain boundaries of the main minerals and elongated along the main schistosity (Fig. 4d).

SEM micrographs of graphite show similar morphologies (Fig. 5). Sample A8 shows a particularly characteristic cluster of flaky graphite plates (Fig. 5a). Intra-granular graphite in carbonates also shows flaky crystals (sample C4, Fig. 5b-d). No fibrous graphite morphology was observed. Some graphite crystals might be hexagonal (Fig. 5d), but those crystals most likely

correspond to other flaky crystals differently oriented or distorted. Thus, besides amorphous carbon, graphite morphology in our samples mainly displays flaky crystals.

3.2.2 Validation of the new SEM-BSE technique

A total of 15 graphitic phyllite samples from the five sites were analyzed for TOC content by both SEM-BSE and CHNS techniques. To compare the mass ratio from the CHNS analyzer with the volume fraction from SEM-BSE, we calculated a volume ratio α_V based on the measured mass ratio α_m for TOC content determined using the CHNS analyzer, following:

$$\alpha_V = \alpha_m \frac{1-\phi}{\frac{\rho_g}{\rho_m}(1-\alpha_m)+\alpha_m} \quad , \tag{7}$$

where ϕ is the porosity (taken equal to 2 %, as measured on 12 graphitic phyllite samples), and ρ_g and ρ_m are density of graphite (2200 kg m^{-3}) and density of the surrounding mineral matrix (2700 kg m^{-3}, typical of crustal rocks), respectively.

The calculated TOC content from SEM-BSE ranged from 2.6±0.2 to 7.50±0.04 % which is nearly similar to the volumetric TOC content inferred from CHNS analyzer using Eq. (7), with a range from 2.0±0.1 to 8.4±0.5 %. As shown in Fig. 6, a positive correlation is obtained between volumetric TOC content measured by both methods, with a mean relative difference of 7±1 %. Our results show that the SEM-BSE technique is reliable to determine TOC content of graphite-rich rocks. The SEM-BSE method has the advantage of being faster and does not need a long sample preparation of several days as necessary with the CHNS method for sample decarbonation. This new technique, in addition to giving direct estimates of TOC of a sample, provides information on the microstructural position of elemental carbon and allows us to draw a map of graphite occurrences in a sample. Our

SEM-BSE technique could thus be compared with the mapping of carbonaceous material obtained by Raman spectroscopy.

4. Results

The results of each of the five sites (A-E) in the Upper Trisuli valley are shown separately in Figs. 7-11 together with a photograph of the site, and a geological cross-section for sites A and D. All the data are summarized in Table 1 site by site. Additional information, precise location and all available data are presented in Supp. Table S1.

4.1 Results of the reference site A in the Upper Trisuli valley

Site A (Fig. 7a) shows a massive graphitic phyllite outcrop from 2002 to 2031 m asl. extending from positions 68 m to the west to 308 m to the east. A shear zone, sandwiched between two quartzite bands, is observed at position 52 m and separates graphitic phyllite from mica-schist. At the eastern end of the profile, debris flow deposits mainly composed of dolomite and soil are present (Fig. 7c).

Based on a total of 26 samples (from sample A1 to sample A34, including the other sample ME1), this site was extensively studied with sampling space of about 10 m. In addition, the two high-resolution sampling areas are described in Supp. Fig. S13. The $\delta^{13}C$ values of carbon from the bulk (*i.e.* non-decarbonated samples) range from –28.7 to –5.9 ‰, suggesting the occurrence of carbonates in samples with heavy carbon isotope signatures (Fig. 7b). TOC content ranges from 1.8 to 9.0 % with a mean value of 3.9±0.1 % while TC content ranges from 1.8 to 12.6 % with a mean value of 4.2±0.4 %. About two times higher TOC content is observed in the eastern part of the profile near the shear zone rich in gouge with a mean value of 5.2±0.6 % from position 68 to 158 m. IC content is significant in three samples (A1, A4 and A5) with a mean value of 7.2±1.3 %. TOC content decreases

towards the west reaching values smaller than 5 %; IC content remains smaller than 3 % or is negligible. The dispersion of TOC values in the eastern part of the profile (38±10 %; *n*=10) is larger than in the rest of the profile (20±4 %; *n*=15) (Fig. 7b).

Calculated B-RSCM peak-*T* values range from 519 to 590 °C. While they remain relatively homogeneous, slightly higher peak-*T* values are obtained in the eastern part of the profile. The values of D1-, G- and D2-FWHM, with mean values of 43.6±0.6 cm^{-1}, 20.8±0.3 cm^{-1} and 20.3±1.0 cm^{-1}, respectively, show only small spatial variations, with exceptions in the eastern part of the profile (Fig. 7c). These values suggest the presence of moderately crystalline graphite, consistently with previous studies done in Nepal (Beyssac et al., 2004; Bollinger et al., 2004).

4.2 Results of the two nearby sites B and C

Site B (Fig. 8a) shows a graphitic phyllite outcrop from 1886 to 1909 m asl. extending from positions 10 m to the west to 99 m to the east. The profile consists mainly of phyllite without occurrence of carbonate bands, as confirmed by decarbonating the samples and the $\delta^{13}C$ values of carbon from the bulk ranging between –26.6 and –26.1 ‰ (Fig. 8b). The eastern part of the profile marks the contact between mica schist and garnet schist and augen gneiss. TOC content ranges from 1.6 to 5.3 % with a mean value of 3.5±0.6 %, while TC content ranges from 1.4 to 4.4 % with a mean value of 3.0±0.4 %. Calculated B-RSCM peak-*T* values range from 530 to 574 °C with a mean value of 558.7±6.1 °C. They do not show large spatial variations, besides near the contact (Fig. 8b). Only small spatial variations are observed for D1-, G- and D2-FWHM values, with mean values of 40.5±1.0 cm^{-1}, 21.0±0.3 cm^{-1} and 16.9±1.7 cm^{-1}, respectively.

Site C (Fig. 9a) shows a representative graphitic phyllite outcrop extending from positions 0 m to the east to 50 m to the west. The profile is characterized by a clear anomalous contact with 20–

40-cm-thick gouge at position 28 m. To the east of the profile, augen gneiss occurs, while to the west mica-schist crops out. The $\delta^{13}C$ values of carbon from the bulk, ranging between –16.7 and –2.9 ‰, suggest a significant fraction of IC (Fig. 9b). TOC content shows significantly larger values ranging from 1.0 to 7.0 % with a mean value of 2.5±0.8 %, while TC content shows significantly larger values ranging from 6.2 to 10.9 % with a mean value of 9.0±0.7 % (Fig 9b). Conversely, IC content values are larger than at the other sites, except for the gouge sample C4, and range from 1.0 to 9.1 % with a mean value of 6.4±1.1 %. The gouge sample C4 has an exceptionally high TOC content of 7.0±0.4 %, separating rocks with similar TOC contents. Calculated B-RSCM peak-*T* values range from 521 to 581 °C with a mean value of 559.1±8.2 °C. They show large variations in the vicinity of the gouge, with the lowest peak-*T* value obtained for the gouge sample (Fig. 9b). D1-, G- and D2-FWHM values show significant spatial variations in the vicinity of the contact zone and have mean values of 40.3±1.7 cm^{-1}, 20.1±0.8 cm^{-1} and 14.0±1.3 cm^{-1}, respectively.

4.3 Results of the two farther sites D and E

Site D (Fig. 10a) shows a massive graphitic phyllite outcrop extending from positions 30 m to the east to 124 m to the west. The profile is characterized by an alternation of mica-schist with quartz lenses at some locations and graphitic phyllite with a pronounced black color (Fig. 10a,c). The $\delta^{13}C$ values of carbon from the bulk, ranging between –28.7 and –25.5 ‰, suggest no or little carbonate occurrence (Fig. 10b). TOC content shows values similar to sites A and B, ranging from 1.6 to 4.8 % with a mean value of 3.6±0.3 % (Fig. 10b), while TC content shows values ranging from 1.7 to 4.7 % with a mean value of 3.6±0.4 %. IC content is negligible, except for two samples with a small mean value of 0.69±0.02 %. Calculated B-RSCM peak-*T* values range from 542 to 581 °C with a mean value of 565.5±4.2 °C. They are higher in the center of the profile (Fig. 10b). While a slight

increase to the west is observed, D1-, G- and D2-FWHM values remain similar along the profile with mean values of 44.1±0.9 cm^{-1}, 20.5±0.2 cm^{-1} and 16.6±1.8 cm^{-1}, respectively.

Site E (Fig. 11a) shows a slightly weathered graphitic phyllite outcrop extending from positions 3 m to the east to 90 m to the west. The outcropping rock is sometimes hidden by debris fall deposits made of soil. The $\delta^{13}C$ values of carbon from the bulk, ranging between –25.9 and –22.2 ‰, suggest a negligible amount of IC (Fig. 11b). TOC content shows values relatively similar to sites A, B and D, with values ranging from 2.9 to 5.7 % with a mean value of 4.1±0.3 % (Fig. 11b), while TC content shows values ranging from 2.8 to 5.5 % with a mean value of 4.0±0.3 %. TOC content shows higher values above 5 % at positions 3 and 65 m. Calculated B-RSCM peak-*T* values are relatively homogeneous and range from 549 to 575 °C with a mean value of 563.1±2.7 °C. The highest peak-*T* value is also observed at position 65 m (Fig. 11b). D1-, G- and D2-FWHM values are higher to the west of the profile and have mean values of 43.3±0.6 cm^{-1}, 20.6±0.3 cm^{-1} and 13.7±0.7 cm^{-1}, respectively.

4.4 Overview of carbon contents, peak-*T* and $\delta^{13}C$ results in the Upper Trisuli valley

Our extensive data set obtained from the Upper Trisuli valley allows us to study the distribution of the data obtained (Fig. 12). The TOC content (Fig. 12a) ranges from 0.9 to 9.0 %, with an overall mean of 3.7±0.2 %. The distribution is log-normal, with a median of 3.6±0.4 %, close to the mean. In total, 13 samples (15.4 %) have a TOC content above 5 %. The TC content (Fig. 12b) varies over a larger range, between 1.4 and 12.6 %, with a distribution centered on a mode at 2.5 % and showing a long tail toward higher values. Peak-*T* (Fig. 12c) ranges between 518.7 and 556.9 °C with a mean of 556.9±5.9 ºC. Peak-*T* values follow a scattered log-normal distribution centered on the mean, but a long tail toward smaller values is obtained. Regardless the considered site, besides

few outliers, the G-band wavelength and FWHM are gathered around a characteristic mean value of 1579.8±0.2 cm^{-1} and 20.7±0.2 cm^{-1}, respectively. Similarly, the data show similar both D1/G FWHM ratio and D1/G intensity ratio, suggesting relatively homogeneous metamorphic conditions for all the studied samples (Supp. Fig. S14). Based on 20 analyses, the $\delta^{13}C$ values of the non-decarbonated graphitic phyllite samples range between –2.9±0.1 and –28.7±0.1 ‰, with a mean of –22.0±0.1 ‰ (Fig. 12d). $\delta^{13}C$ values show a main mode at –25 ‰, typical of organic carbon, and a secondary mode around –5 ‰, suggesting mixing with the carbonate source.

Considering the whole set of samples from the Upper Trishuli Valley, the presence of IC content is negligible for most of the samples (Fig 13a). Nine samples show IC content above 5 % and relatively low TOC content, most of them belonging to site C. Some samples show the combination of TOC and IC with similar TOC and IC contents. Most of the samples analyzed for $\delta^{13}C$ from all the outcrops show negligible IC content (Fig. 13b), large TOC content (Fig. 13c) and $\delta^{13}C$ values lower than –20 ‰ (Fig 13b,c), indicating the predominance of organic carbon. Four samples have large IC content and higher $\delta^{13}C$ values (mean: –5.1±0.1 ‰). One sample from site C shows an intermediate $\delta^{13}C$ value of –16.7±0.1 % and an IC content of about 1 %, suggesting a mixing of organic and inorganic carbon (Fig. 13b,d). When TC content is large, above 7 %, in most of the cases IC content is non-negligible. Decarbonated samples show more negative $\delta^{13}C$ values (Fig. 13c,d), confirming that most of the carbonates, if not all, were removed. These observations clearly indicate that, despite the fact that the samples were collected in the field with the utmost caution to avoid carbonates, some of them bear carbonates in non-negligible amount. This suggests that even in the case of no visible carbonate band(s) in the field, it appears of the utmost importance to systematically study bulk and decarbonated samples.

4.5. Complementary results from Far-Western to Eastern Nepal

The results obtained on the 67 samples collected from other valleys from Far-Western to Eastern Nepal are summarized in Table 2. Additional information, precise location and all available data are presented in Supp. Table S1.

In other valleys of Central Nepal, in the Ankhu valley to the west and in the Bhote Koshi valley to the east, high TOC content is also obtained with most values above 1 % and the maximum value of 10.4±0.4 %. In Western Nepal, in Kali Gandaki and Marsyandi valleys and at Barpak location (Gorkha district) large TOC contents are obtained with mean values above 3 %, relatively consistent with large values already reported in Marsyandi and Kali Gandaki valleys (Evans et al., 2008; Paudel, 2011). In Eastern Nepal, in the areas of Akhuwatar and Leute, TOC contents reach values above 4 to 5 %. By contrast, in Far-Western Nepal, samples from Baitadi-Darchula and Jumla-Humla sections show relatively small TOC contents ranging from <0.1 to 2 %. In Mid-Western Nepal, in Lower Dolpo, TOC content appears even smaller with values from 0.2 to 1.1 %. These data suggest some coherence and heterogeneity at various spatial scales.

5. Discussion

From the results presented above, we discuss: first, the significance of the data at increasing spatial scales, from metric, kilometric and to larger scales; second, the relationship between carbon content and peak-*T* and their general patterns; and third, the carbon isotopic signatures. Finally, we discuss the possible implications for our understanding of the carbon reservoirs in the Himalaya.

5.1. Coherence of metamorphic conditions at increasing spatial scales

5.1.1. Sample to metric and decametric scale variations of metamorphic conditions

In our study, several samples were divided into 3-4 subsamples and analyzed, as detailed in section 3 above ('Sample analysis'). Here, we define the sample-scale dispersion (SASD) as the standard deviation of a parameter obtained over a set of subsamples of the same original sample, and divided by the mean value and expressed in per cent. On average, SASD for TOC content amounts to 46±19 %, while it is 2.90±0.01 % for peak-*T* (Table 1). The SASD value for TOC is large, slightly larger than other SASD obtained for other parameters from similar samples (Girault and Perrier, 2012), and suggests that large differences can be observed at small spatial scale. At this small spatial scale, the organic matter precursor is probably the same. Albeit difficult to explain, the heterogeneity might be due to non-homogeneous distribution of organic matter in the sedimentary protolith rock, frozen during metamorphism.

At meter-scale, as shown in Supp. Fig. S12 for the two high-resolution sampling areas, larger dispersion of values is obtained for HR1. Here, we define the scarp-scale dispersion (SCSD) as the standard deviation of a parameter obtained over a set of samples located up to a few meters from each other, and divided by the mean value and expressed in per cent. At meter-scale, considering the high-resolution sampling area HR2, SCSD values of TOC content and peak-*T* amount to 24.3±5.5 % and 2.18±0.01 %, respectively (Table 1). The SCSD value for peak-*T* is small, consistent with a study testing for peak-*T* representativeness at a scale of 2–3 m (Umeda and Enami, 2014). The SCSD value for TOC is smaller than SASD values, but relatively similar to other SCSD values inferred from other parameters (Girault and Perrier, 2012). By contrast, considering the high-resolution sampling area HR1, SCSD values of TOC content and peak-*T* amount to 48±13 % and 2.86±0.02 %, respectively (Table 1). The SCSD value for TOC is larger than SCSD generally obtained for other parameters in similar context as mentioned above. At such meter scale, similar effects considered for SASD can be considered, and might be even more pronounced. Due to these SCSD values, the collection of one

sample per outcrop only might be risky in terms of larger scale interpretation for carbon content, and poses the question of the representativeness of a given sample.

This is emphasized by the SCSD values obtained for 10-m-spaced samples at each of the five studied sites (Figs. 7-11). The dispersion of TOC content is shown in Fig. 14 separately for all the five sites. SCSD values for TOC at the scale of an outcrop remain compatible with SCSD values obtained for 1-m distance with values ranging generally from 20.3±4.7 % (site E) to 41.2±5.1 % (site A). However, site C shows a particularly large SCSD value for TOC (81±33 %), due to the occurrence of fault gouge. SCSD appears larger when the number of samples is greater, but remains generally specific for a given site. It is less pronounced for peak-*T* values (Supp. Fig. S7 and Fig. 14). While TOC content appears mainly dependent on the distribution of organic matter in the protolith, which may differ between outcrops of the same formation, peak-*T* values are more homogeneous at the scale of an outcrop, and tend to reflect the overall metamorphic conditions. Thus, based on the available data, to obtain a representative peak-*T* value for a given outcrop, a few samples only appear sufficient. By contrast, heterogeneities at different spatial scales impede obtaining a representative TOC content value at the outcrop scale when collecting less than 10 samples.

5.1.2. Unit-scale to large scale variations of metamorphic conditions

When considering all the five sites (A-E) of the same unit in the Upper Trisuli valley (Tables 1 and 2), we define the unit-scale dispersion (UNSD) as the standard deviation of a parameter obtained over a set of samples located within the same geological unit or formation, and divided by the mean value and expressed in per cent. Over the 7-km-long outcrop of the graphitic mica-schist unit we studied, UNSD values for TOC content (40.8±3.9 %) and peak-*T* values (2.58±0.01 %) are larger than SASD and, on average, larger than SCSD. Dispersion of values thus depends on the considered spatial scale.

Increasing again the spatial scale of observation, the graphitic mica-schist unit is encountered in the upper-LHS south to MCT at several locations throughout the Nepal Himalaya. For peak-*T* values, from Far-Western to Eastern Nepal, we consider our original data-set from the Upper Trisuli valley and from other valleys of Nepal, complemented by published data (Beyssac et al., 2004; Bollinger et al., 2004; Evans et al., 2008; Paudel, 2011). Data are summarized in Table 2 and illustrated in a regional map in Fig. 15. All over this 800-km-long lateral portion of the Himalaya, peak-*T* values range from 514.3±13.5 °C in Far-Western Nepal to 536.3±9.6 °C in Central Nepal. UNSD amounts to 3.6±0.7 % for peak-*T* values. This value is similar to UNSD obtained at km-scale and indicates that the whole unit is representative of the large-scale metamorphic conditions south to MCT. Small along-strike variations in peak-*T* values at the scale of the Nepal Himalaya suggest similar thermal history of graphitic phyllites. Little carbon content data are available all over the Nepal Himalaya. When considering the available TOC data, with only 58 data from outside Central Nepal, a large UNSD value of 60.5±4.9 % is obtained for TOC and suggests the need for additional measurements.

Outside Nepal, at the scale of the Himalaya, graphitic phyllite is probably encountered from Bhutan to Zanskar, a few kilometers south to MCT. Little is known on graphitic phyllite occurrences, but inferences from several studies focusing on the thermal metamorphism of the LHS rocks south to MCT reported similar ranges of values for peak-*T*, *e.g.*, in Eastern and Central Bhutan (Long et al., 2016; Grujic et al., 2020) and in Western India (Célérier et al., 2009; Rawat and Sharma, 2011; Mathew et al., 2013). Despite the scarcity of available data, TOC content with a mean value of 1.7±0.3 % in the Larji-Rampur window, Himachal Himalaya, India (Rana et al., 2021) appears smaller than TOC content obtained in Nepal. These observations denote a large-scale thermal metamorphism that encompasses the whole Himalayan range and suggest a large-scale overall coherence of metamorphic conditions for the Himalayan graphite from the upper-LHS over the orogeny, with possible smooth variations, especially at the edges.

5.2 Carbon content versus peak-*T* and the highest peak-*T* attained by upper-LHS rocks

In the studied graphitic phyllite samples, peak-*T* indicates the thermal history and the carbon content constrains the amount of carbon stored as graphite. Using both complementary parameters will improve our understanding of the relationship between metamorphism releasing carbon and the storage of carbon in the form of graphite. In Fig. 14, TOC content is plotted as a function of peak-*T* for our sample set. The samples from sites B, C, D and E are clustered and fall into the bottom part of the carbon domain. Site A shows more scattered data. Mean peak-*T* is relatively similar for all sites. The sites A, B, C, D and E are located at an approximate structural distance to MCT of *ca.* 2.9, 2.7, 3.2, 2.2 and 3.6 km, respectively. No clear relationship is observed between TOC and peak-*T* with the distance to the MCT at this spatial scale. From site A and C, higher carbon content tends to imply higher peak-*T* (Fig. 14). This might depend upon the kinetic of recrystallization of graphite crystals. Indeed, the presence of evident D1 peaks in all our samples suggests that the degree of graphite crystallinity remains low. Thus, graphite in our samples likely derives from progressive recrystallization of carbonaceous material at increasing temperature during prograde metamorphism. This confirms that the graphitic phyllites are the metamorphic products of sedimentary protoliths rich in organic matter deposited all along the northern margin of the Indian plate. In the context of the MCT zone where no methane has been reported so far, the potential formation of hydrothermal graphite, deposited from COH fluids, remains unlikely at this stage (Craw and Upton, 2014). Indeed, if graphite would have been deposited from COH fluids, we would not expect its systematic occurrence within a specific stratigraphic formation, but instead punctual occurrences controlled by fluid pathways.

In our sample set, the lowest and highest peak-*T* values determined by B-RSCM technique reach 518.7±8.5 °C and 589.9±8.2 °C, respectively. The highest peak-*T* values are obtained at site A,

near the fault zone. At the other sites, high peak-*T* values are also obtained, with two values above 580 °C at sites C and D. These high peak-*T* values are below the upper limit of the RSCM method, which has been extended to 640 °C (Beyssac et al., 2016; Delchini et al., 2016). These values are among the highest RSCM-based peak-*T* ever recorded by upper-LHS rocks in Nepal: the highest published values were 571.8±9.0 °C along the Bhote Koshi valley near Kodari, Central Nepal and 568.5±16.0 °C along the Khudi valley near the Marsyandi valley, Western Nepal (Beyssac et al., 2004). As shown in the Nepal map (Fig. 15) and summarized in Table 2, both the highest mean peak-*T* and carbon content values are obtained in Central Nepal. Progressively decreasing carbon content and peak-*T* values are reported towards Western, Mid-Western and up to Far-Western Nepal. Outside Nepal, peak-*T* reaches about 568 °C in Kumaun, Western India (Rawat and Sharma, 2011; obtained using B-RSCM), about 574–582 °C in Bhutan (Long et al., 2016; corrected from R-RSCM using our Supp. Fig. S5) and about 600–617 °C in Arunachal Himalaya (Mathew et al., 2013; obtained using B-RSCM). Thus, peak-*T* values obtained in Nepal are higher than those obtained in Western India and lower than those obtained in Bhutan and Eastern India. The available data so far might suggest an increase of the highest peak-*T* of upper-LHS rocks from west to east along the Himalayan belt, but this preliminary inference needs to be confirmed with further data along strike.

We have shown that the graphitic mica-schist unit of the upper-LHS experienced RSCM-based metamorphic temperatures slightly higher than those previously estimated. This suggests that, based on peak-*T* only, the transition between LHS and GHS rocks is rather narrow, and that it may depend on the location along the strike of the Himalayan orogen. Generally, the peak-*T* difference between LHS and GHS is about 50 to 100 °C (Bollinger et al., 2004); actually, this difference could be smaller, of the order of only 30 °C. More interestingly, at the footwall of the MCT over the Nepal Himalaya, our peak-*T* data inferred from the RSCM approach, together with published RSCM-based peak-*T* values, substantially confirm the temperature constraints obtained using the equilibrium thermodynamics approach from Nanga Parbat to Namche Barwa (Goscombe et al., 2018).

Furthermore, the possible eastward increase of our peak-*T* values appears similar to the slightly higher temperature towards East as reported by Goscombe et al. (2018). The high inferred peak-*T* indicates that graphitic phyllites were subjected to higher temperature, while the pressure might have remained relatively similar to other adjacent rocks. This may indicate that the distorted isotherms at depth near the MCT zone (*e.g.*, Herman et al., 2010; Wang et al., 2022) were already there at least 5 Ma years ago when MCT was highly active during Himalayan orogeny. Such modified isotherms may have promoted heating of rocks and fluids, leading to surface manifestations such as hot springs and CO_2 degassing areas, similar to or even enhanced while compared with current observations (*e.g.*, Girault et al., 2014, 2018, in press a,b). More data are needed to substantiate this interpretation further, and its consequences in terms of alteration.

5.3 Carbon isotopic composition signatures of graphitic phyllites

The bulk carbon isotopic composition ($\delta^{13}C$) of the graphitic phyllites is relatively homogeneous, with almost all values around the mean (–22.0±0.1 ‰) and 75 % of our data with $\delta^{13}C$ value of *ca.* –26 ‰, suggesting a biogenic carbon origin of the graphite in Central Nepal (Fig. 13), as already reported in Western Nepal (*e.g.*, Evans et al., 2008). The outliers have less negative $\delta^{13}C$ values around –5 ‰ (samples A4, C1, C5 and C7) and one intermediate value around –16 ‰ (sample C4), as also reported in Himachal Pradesh (Rana et al., 2021). Graphitic phyllite after removing carbonates yield more negative $\delta^{13}C$ values, suggesting the presence of carbonates in the samples. Analysis of carbon isotopic composition of a dolomite sample belonging to the same lithological unit gave $\delta^{13}C$ of –1.3±0.1 ‰ (and $\delta^{18}O$ of –15.0±0.7 ‰), consistent with other published $\delta^{13}C$ values of *ca.* –2 ‰ for carbonates in metapelites (Evans et al., 2008).

This variability in our $\delta^{13}C$ values and the significant negative shift of the carbonate $\delta^{13}C$ signature remain difficult to explain. However, such inconsistent $\delta^{13}C$ values have also been reported

and discussed in other orogenic belts (Kiran et al., 2022) and may be more general (Fig. 16). Indeed, while most of $\delta^{13}C$ values from graphitic rocks in orogenic belts remain generally close to the overall mean value of –23±4 ‰, more negative values (Hoefs and Frey, 1976; Rodas et al., 2000; Evans et al., 2008; Barrenechea et al., 2009; Sharma et al., 2011; Neubeck et al., 2020; Rana et al., 2021) and outliers with less negative values are sometimes reported (Hoefs and Frey, 1976; Baker, 1988; Sanyal et al., 2009; Taner et al., 2017; Rana et al., 2021; Li et al., 2022).

Carbon isotope fractionation between calcite and graphite, $\Delta_{(Cc\text{-}Gr)}$, is expected to decrease with increasing temperature (Valley and O'Neil, 1981, Fig. 2; Satish-Kumar et al., 2002, 2011; Kiran et al., 2022). Hence, the low $\delta^{13}C$ of most of the graphitic phyllites is consistent with the quasi-absence of carbonates at high temperature. However, the high $\delta^{13}C$ outliers (samples A4, C1, C5 and C7) are characterized by high IC contents (Fig. 13b) and $\delta^{13}C$ values after removing carbonates are lower than TC values. This suggests re-equilibration during metamorphism between organic carbon and pre-existing sedimentary carbonates. These samples have organic carbon fraction between 0.19 and 0.27. Assuming a protholith with organic carbon fraction of 0.25 with $\delta^{13}C$ of –25±1 ‰ and carbonate with $\delta^{13}C$ of –1.3±0.1 ‰ would lead to a bulk composition of *ca.* –7±1 ‰ using a mass balance approach. This value appears compatible with the range of observed values for three of the outliers. Sample C7 with a measured $\delta^{13}C$ value from the bulk of –2.9 ‰ may imply an open system re-equilibration in a carbonate-rich environment. This is compatible with our petrographic observations that do not show evidence for equilibria between calcite and graphite in our samples. Similarly, no clear relation between Raman-based peak-*T* and $\delta^{13}C$ is observed (Supp. Fig. S15), suggesting that these outliers with high $\delta^{13}C$ values are not related to deep metamorphic processes (*e.g.*, devolatilization, see Nakamura et al., 2015, 2018, 2020).

5.4 Implications for the carbon reservoirs in the Himalaya

In the Upper Trisuli valley, to the west in the Ankhu valley ("Ruby valley"), and to the east in the Bhote Koshi valley, Central Nepal, a large number of graphitic phyllites from the graphitic mica-schist unit were collected (n=96). They gave relatively high TOC contents with values ranging from 0.6 % to 10.4 % and with a mean value of 3.5±0.2 %. These three valleys are an important starting point to quantify the amount of organic carbon stored as graphite and to compare it with the carbonates reservoir. Here, to simplify, we consider the unit as a whole, characterized by both organic and inorganic carbon. Based on the work by Tamang (2022), we use the average and min-max range of vol.% values for carbonate-bearing lithologies in the unit. Using estimated thicknesses for the unit (DeCelles et al., 2001; Robinson et al., 2006) and considering also the shortening of the upper-LHS rocks (Long and Robinson, 2021), we can give first estimates of the amount of organic carbon and of the fraction of organic carbon compared with total carbon stored in the unit.

In Central Nepal, for the graphitic mica-schist unit, we take 3–4 km thickness of upper-LHS rocks, 50,400±6400 km^2 reconstructed surface area, 26±9 vol.% of carbonates and mean (min–max range) for TOC content of 3.5±0.2 % (0.9–10.4 %). We obtain a total amount of organic carbon of (1.4±0.3)×10^7 Mton, representing about 10±4 % of the total carbon amount in the unit. Considering maximum ranges of values yield an estimated fraction of organic carbon of *ca.* 20 %. Extrapolating this calculation to Eastern and Western Nepal, using the measured TOC content in this study and other parameters from the aforementioned literature, we can calculate in the same manner the amount and fraction of organic carbon in Eastern and Western Nepal. Smaller amounts of TOC are obtained, (8±5)×10^6 Mton for Western Nepal and (1.5±0.6)×10^6 Mton for Eastern Nepal, which lead to mean TOC fraction of 8 % and 6 % and maximum TOC fraction of *ca.* 16 % and 11 %, respectively. Thus, at the scale of the upper-LHS rocks in Nepal, the TOC content may represent from 10 to 20 % of the total carbon stored. As similarly evidenced in the case of subduction (Plank and Manning, 2019), graphite emerges as an important carbon reservoir possibly representing from one-tenth to one-fifth of the total carbon stored during collision.

As illustrated in the cross-section, oriented south to north and crossing the Kathmandu Klippe, the graphitic mica-schist unit in the upper-LHS was folded and currently crops out at the surface at three locations (Fig. 17): above the Main Boundary Thrust (MBT), north to the Klippe and in the MCT zone. This particular unit bearing graphite appears to be associated with the major thrust faults of the Himalayan orogeny, and, due to its lubricant behavior, it may control the dip direction of the main thrusts and faults participating to the shortening, govern the underplating and reduce the friction on fault planes (*e.g.*, Parnell and Brolly, 2021; Parnell et al., 2021). In addition, in the MCT zone, and in a smaller part in the MBT zone, numerous hydrothermal systems bearing hot springs, that release varying amounts of CO_2 of metamorphic origin, are reported (*e.g.*, Becker et al., 2008; Evans et al., 2008; Girault et al., 2014, 2018, 2022, in press a,b). The CO_2, whose production was initiated as soon as the collision provided the necessary temperature and pressure, is still currently produced by decarbonation reactions at depth, mainly in the LHS rocks beneath the MCT (Tamang, 2022), and in the GHS rocks in a smaller part (*e.g.*, Groppo et al., 2013, 2022; Rapa et al., 2017). The stored graphite-rich layer may act as a barrier for the upward percolation of the deeply produced metamorphic CO_2-rich fluids. Conversely, it may channelize the current release of CO_2 toward the surface, and probably also the past CO_2 emissions (Guo et al., 2021). Central Nepal, which can be considered as the generic example, exhibits the highest organic carbon content in the form of graphite, the highest peak-*T*, and the highest current CO_2 emission.

Central Nepal also shows the smallest recurrence time for large earthquakes (*e.g.*, Bollinger et al., 2014). It was also the rupture zone of the 2015 M_w 7.9 Gorkha earthquake and its aftershocks (Adhikari et al., 2023). The large-scale coherence of our observations and the systematic association of thick graphitic layers with current CO_2 emissions can hardly be coincidental and suggests possible connections between organic carbon stored as graphite and mobile inorganic carbon released as CO_2 at the scale of the Himalayan orogenic belt, an important aspect to be investigated further for global

carbon budget estimations (Kelemen and Manning, 2015; Plank and Manning, 2019; Müller et al., 2022).

6. Conclusion

In this paper, using various methods to characterize and quantify graphitic carbon content, including a new SEM-BSE technique, we have shown that graphitic phyllites of the Upper Lesser Himalaya are significant components when investigating the metamorphic conditions in the MCT zone at the scale of the whole Himalayan orogen. Our data in the Upper Trisuli valley, Central Nepal have shown a significant coherence of the metamorphic conditions at small to large spatial scales (flaky graphite characteristics, peak metamorphic temperature and carbon isotopic composition), but also show some discrepancies between $\delta^{13}C$ of phyllites, suggesting metamorphic re-equilibration between organic carbon and carbonates in samples with high $\delta^{13}C$. The addition of complementary data from other valleys from Far-Western to Eastern Nepal have allowed us to map along strike the metamorphic conditions of upper-LHS rocks. Higher TOC content and peak-*T* values have been observed in Central Nepal. Our results thus establish a robust framework for the understanding of the carbon stored in orogenic belts, an essential component of the global carbon budget.

Our study is the first multiscale systematic investigation of graphitic phyllites from the upper-LHS, conducted at a scale which is order of magnitude more detailed than that of previous studies. The new technique based on SEM-BSE for estimating TOC would now benefit from more case studies on other types of metamorphic rocks with more crystalline graphite, such as those formed in hydrothermal veins. Although the graphite in upper-LHS rocks is moderately crystalline, due to its widespread occurrence along the MCT zone, it might represent an important economic asset for the country. However, more effort is needed to better characterize its industrial potential (Paudel, 2011; Palosaari et al., 2016; Robinson et al., 2017).

We have shown that in the context of the deep carbon cycle, Himalayan graphitic phyllites represent a major reservoir of organic carbon in the Himalaya, in addition to inorganic carbon reservoir of carbonate-bearing lithologies. The fraction of organic carbon may represent up to 20 % of the total carbon stored. The main difference with respect to carbonates, is that graphite is much more stable than carbonates during prograde metamorphism and through weathering, making it a long term sink in the carbon cycle. While carbonates experience decarbonation reactions as temperature and pressure progressively increase, graphite remains passively stable, simply increasing its degree of crystallinity and not being involved in CO_2-producing or CO_2-consuming reactions. Thus, this graphitic mica-schist unit, encountered from Bhutan to Zanskar, is a remarkable sign of the carbon sink/source duality of the Himalayan orogeny (Gaillardet and Galy, 2008), and emerges as a key marker to study when working on the global carbon budget.

Acknowledgments

We thank Som Nath Sapkota, the Department of Mines and Geology, and in particular Mukunda Bhattarai and Rajesh Sharma from the National Earthquake Monitoring and Research Center (DMG/NEMRC) for their support. We thank Sudhan Singh Mahat and Sanjen Jalavidhyut Company Limited for their precious help at site D (Sanjen outcrop). Om Bahadur Tarum, Dawa Tamang, and Niraj Jairu are thanked for assistance in the field. We thank Laurent Bollinger for fruitful discussions. We thank Emmanuelle Raimbault for measurement of carbon content in IPGP and Philippe Blanc (LithoB) for preparation of thin sections. We are thankful to the Editor Balz Kamber, Madhusoodhan Satish-Kumar and an anonymous reviewer for thorough reviews which significantly improved the initial version of the manuscript. Financial support was provided by funding of the IPGP team "Physics of Natural Sites", complemented by a LabEx UnivEarthS Frontier funding "MYSTHIC" (ANR-10-LABX-0023 and ANR-18-IDEX-0001) lead by F.G.

References

Adhikari, L.B., Laporte, M., Bollinger, L., Vergne, J., Lambotte, S., Koirala, B.P., Bhattarai, M., Timsina, C., Gupta, R.M., Wendling-Vazquez, N., Batteux, D., Lyon-Caen, H., Gaudemer, Y., Bernard, P., Perrier, F., 2023. Seismically active structures of the Main Himalayan Thrust revealed before, during and after the 2015 M_w 7.9 Gorkha earthquake in Nepal. Geophys. J. Int. 232, 451-471.

Ague, J.J., 2000. Release of CO_2 from carbonate rocks during regional metamorphism of lithologically heterogeneous crust. Geology 28, 1123–1126.

Amatya, K.M., Jnawali, B.M., 1994. Geological Map of Nepal (scale: 1:1,000,000). Department of Mines and Geology, Kathmandu.

Aoya, M., Kouketsu, Y., Endo, S., Shimizu, H., Mizukami, T., Nakamura, D., Wallis, S., 2010. Extending the applicability of the Raman carbonaceous-material geothermometer using data from contact metamorphic rocks. J. Metamorph. Geol. 28, 895–914.

Arora B. R., Unsworth, M.J., Rawat, G., 2007. Deep resistivity structure of the northwest Indian Himalaya and its tectonic implications. Geophys. Res. Lett. 34, L04307.

Arita, K., 1983. Origin of the inverted metamorphism of the lower Himalayas, Central Nepal. Tectonophysics 95, 43–60.

Arita, K., Shiraishi, K., Hayashi, D., 1984. Geology of western Nepal and a comparison with Kumaun, India. J. Fac. Sci. Hokkaido Univ. Ser. IV 21, 1–20.

Avouac, J.-P., 2003. Mountain building, erosion, and the seismic cycle in the Nepal Himalaya. Adv. Geophys. 46, 1–80.

Baker, A.J., 1988. Stable isotope evidence for limited fluid infiltration of deep crustal rocks from the Ivrea Zone, Italy. Geology 16, 492–495.

Barrenechea, J.F., Luque, F.J., Millward, D., Ortega, L., Beyssac, O., Rodas, M., 2009. Graphite morphologies from the Borrowdale deposit (NW England, UK): Raman and SIMS data. Contrib. Mineral. Petrol. 158, 37–51.

Becker, J.A., Bickle, M.J., Galy, A., Holland, T.J.B., 2008. Himalayan metamorphic CO_2 fluxes: Quantitative constraints from hydrothermal springs. Earth Planet. Sci. Lett. 265, 616–629.

Beyssac, O., Goffé, B., Chopin, C., Rouzaud, J.N., 2002. Raman spectra of carbonaceous material in metasediments: a new geothermometer. J. Metamorph. Geol. 20, 859–871.

Beyssac, O., Goffé, B., Petitet, J.-P., Froigneux, E., Moreau, M., Rouzaud, J.-N., 2003. On the characterization of disordered and heterogeneous carbonaceous materials by Raman spectroscopy. Spectrochim. Acta A Mol. Biomol. Spectrosc. 59, 2267–2276.

Beyssac, O., Bollinger, L., Avouac, J.-P., Goffé, B., 2004. Thermal metamorphism in the lesser Himalaya of Nepal determined from Raman spectroscopy of carbonaceous material. Earth Planet. Sci. Lett. 225, 233–241.

Beyssac, O., Cox, S.C., Vry, J., Herman, F., 2016. Peak metamorphic temperature and thermal history of the Southern Alps (New Zealand). Tectonophysics 676, 229–249.

Beyssac, O., Rumble, D., 2014. Graphitic carbon: A ubiquitous, diverse, and useful geomaterial. Elements, 10, 415–420.

Bollinger, L., Avouac, J.P., Beyssac, O., Catlos, E.J., Harrison, T.M., Grove, M., Goffé, B., Sapkota, S., 2004. Thermal structure and exhumation history of the Lesser Himalaya in central Nepal: Thermal structure of the Lesser Himalaya. Tectonics 23, TC5015.

Bollinger, L., Sapkota, S.N., Tapponnier, P., Klinger, Y., Rizza, M., Van der Woerd, J., Tiwari, D.R., Pandey, R., 2014. Estimating the return times of great Himalayan earthquakes in Eastern Nepal: evidence from the Patu and Bardibas strands of the Main Frontal Thrust. J. Geophys. Res. Solid Earth 119, 7123–7163.

Börner, J.H., Girault, F., Bhattarai, M., Adhikari, L.B., Deldicque, D., Perrier, F., Spitzer, K., 2018. Anomalous complex electrical conductivity of a graphitic black schist from the Himalayas of Central Nepal. Geophys. Res. Lett. 45, 3984–3993.

Bouilhol, P., Debret, B., Inglis, E.C., Burton, K.W., Grocolas, T., Rigaudier, T., Villeneuve, J., 2022. Decoupling behavior of inorganic and organic carbon during slab mantle devolatilization. *Nat. Comm.* 13, 308.

Buseck, P.R., Huang, B.-J., 1985. Conversion of carbonaceous material to graphite during metamorphism. Geochim. Cosmochim. Acta 49, 2003–2016.

Buseck, P.R., Beyssac, O., 2014. From organic matter to graphite: Graphitization. Elements 10, 421–426.

Célérier, J., Harrison, T.M., Beyssac, O., Herman, F., Dunlap, W.J., Webb, A.A.G., 2009. The Kumaun and Garwhal Lesser Himalaya, India: Part 2. Thermal and deformation histories. Geol. Soc. Am. Bull. 121, 1281–1297.

Connolly, J.A.D, Cesare, B., 1993. C-O-H-S fluid composition and oxygen fugacity in graphitic metapelities. J. Metamorph. Geol. 11, 379–388.

Craw, D., Upton, P., 2014. Graphite reaction weakening of fault rocks, and uplift of the Annapurna Himal, central Nepal. Geosphere 10, 720–731.

Debret, B., Ménez, B., Walter, B., Bouquerel, H., Bouilhol, P., Mattielli, N., Pisapia, C., Rigaudier, T., Williams, H., 2022. High-pressure synthesis and storage of solid organic compounds in active subduction zones. Sci. Adv. 8, 37.

DeCelles, P.G., Robinson, D.M., Quade, J., Ojha, T.P., Garzione, C.N., Copeland, P., Upreti, B.N., 2001. Stratigraphy, structure, and tectonic evolution of the Himalayan fold-thrust belt in western Nepal. Tectonics 20, 487–509.

Delchini, S., Lahfid, A., Plunder, A., Michard, A., 2016. Applicability of the RSCM geothermometry approach in a complex tectono-metamorphic context: The Jebilet massif case study (Variscan Belt, Morocco). Lithos 256–257, 1–12.

Dhital, M.R., 2015. Geology of the Nepal Himalaya. Regional Perspective of the Classic Collided Orogen. Springer International Publishing, Switzerland.

Diessel, C.F.K., Brothers, R.N., Black, P.M., 1978. Coalification and graphitization in high-pressure schists in New Caledonia. Contrib. Mineral. Petrol. 68, 63–78.

Dobner, A., Graf, W., Hahn-Weinheimer, P., Hirner, A., 1978. Stable carbon isotopes of graphite from Bogala Mine, Sri Lanka. Lithos 11, 251–255.

Evans, M.J., Derry, L.A., France-Lanord, C., 2008. Degassing of metamorphic carbon dioxide from the Nepal Himalaya. Geochemistry Geophys. Geosystems 9, Q04021.

From, R., Larson, K., 2014. Tectonostratigraphy, deformation, and metamorphism of the Himalayan mid-crust exposed in the Likhu Khola region, east-central Nepal. Geosphere 10, 292–307.

Fujisaki, W., Matsui, Y., Ueda, H., Sawaki, Y., Suzuki, K., Maruoka, T., 2021. Pre-treatment methods for accurate determination of total nitrogen and organic carbon contents and their stable Isotopic compositions: Re-evaluation from geological reference materials. Geostand. Geoanal. Res. 46, 5–19.

Gaillardet, J., Galy, A., 2008. Himalaya—Carbon sink or source? Science 320, 1727–1728.

Galvez, M.E., Beyssac, O., Martinez, I., Benzerara, K., Chaduteau, C., Malvoisin, B., Malavieille, J., 2013. Graphite formation by carbonate reduction during subduction. Nat. Geosci. 6, 473–477.

Girault, F., Perrier, F., 2012. Measuring effective radium concentration with large numbers of samples. Part II – General properties and representativity. J. Environ. Radioact. 113, 189–202.

Girault, F., Adhikari, L.B., France-Lanord, C., Agrinier, P., Koirala, B.P., Bhattarai, M., Mahat, S.S., Groppo, C., Rolfo, F., Bollinger, L., Perrier, F., 2018. Persistent CO_2 emissions and hydrothermal unrest following the 2015 earthquake in Nepal. Nat. Comm. 9, 2956.

Girault, F., Bollinger, L., Bhattarai, M., Koirala, B.P., France-Lanord, C., Rajaure, S., Gaillardet, J., Fort, M., Sapkota, S.N., Perrier, F., 2014. Large-scale organization of carbon dioxide discharge in the Nepal Himalayas. Geophys. Res. Lett. 41, 6358–6366.

Girault, F., France-Lanord, C., Adhikari, L.B., Upreti, B.N., Paudyal, K.R., Gajurel, A.P., Agrinier, P., Losno, R., Thapa, S., Tamang, S., Mahat, S.S., Bhattarai, M., Koirala, B.P., Gupta, R.M., Maharjan, K., Tamang, N.G., Bouquerel, H., Gaillardet, J., Bollinger, M., Prevot, F., Chaduteau, C., Rigaudier, T., Assayag, N., Perrier, F., in press a. Volume 1, Chapter 8: Overview of hydrothermal systems in the Nepal Himalaya, in: Cattin, R., Epard, J.-L. (Eds.), Himalaya, dynamics of a giant. ISTE Editions 2022.

Girault, F., France-Lanord, C., Adhikari, L.B., Upreti, B.N., Paudyal, K.R., Gajurel, A.P., Agrinier, P., Losno, R., Groppo, C., Rolfo, F., Thapa, S., Tamang, S., Perrier, F., in press b. Volume 3, Chapter 9: Crustal fluids in the Nepal Himalaya and sensitivity to the earthquake cycle, in: Cattin, R., Epard, J.-L. (Eds.), Himalaya, dynamics of a giant. ISTE Editions 2022.

Girault, F., Perrier, F., Gajurel, A.P., Bhattarai, M., Koirala, B.P., Bollinger, L., Fort, M., France-Lanord, C., 2012. Effective radium concentration across the Main Central Thrust in the Nepal Himalayas. Geochim. Cosmochim. Acta 98, 203–227.

Girault, F., Viveiros, F., Silva, C., Thapa, S., Pacheco, J.E., Adhikari, L.B., Bhattarai, M., Koirala, B.P., Agrinier, P., France-Lanord, C., Zanon, V., Vandemeulebrouck, J., Byrdina, S., Perrier, F., 2022. Radon signature of CO_2 flux constrains the depth of degassing: Furnas volcano (Azores, Portugal) versus Syabru-Bensi (Nepal Himalayas). Sci. Rep. 12, 10837.

Goscombe, B., Gray, D., Hand, M., 2006. Crustal architecture of the Himalayan metamorphic front in eastern Nepal. Gondwana Res. 10, 232–255.

Goscombe, B., Gray, D., Foster, D.A., 2018. Metamorphic response to collision in the Central Himalayan Orogen. Gondwana Res. 57, 191–265.

Grew, E.S., 1974. Carbonaceous material in some metamorphic rocks of New England and other areas. J. Geol. 82, 50–73.

Groppo, C., Rolfo, F., Castelli, D., Connolly, J.A.D., 2013. Metamorphic CO_2 production from calc-silicate rocks via garnet-forming reactions in the CFAS–H_2O–CO_2 system. Contrib. Mineral. Petrol. 166, 1655–1675.

Groppo, C., Rolfo, F., Frezzotti, M.L., 2022. CO_2 outgassing during collisional orogeny is facilitated by the generation of immiscible fluids. Commun. Earth Environ. 3, 1–11.

Grujic, D., Ashley, K.T., Coble, M.A., Cottle, J., Kellett, D.A., Larson, K.P., Whipp, D.M., Gao, M., Whynot, N., 2020. Deformational temperatures across the Lesser Himalayan Sequence in Eastern Bhutan and their implications for the deformation history of the Main Central Thrust. Tectonics 39, e2019TC005914.

Guo, Z., Wilson, M., Dingwell, D.B., Liu, J., 2021. India-Asia collision as a driver of atmospheric CO_2 in the Cenozoic. Nat. Comm. 12, 3891.

Hayes, J.M., Waldbauer, J.R., 2006. The carbon cycle and associated redox processes through time. Philos. Trans. R. Soc. Lond., B, Biol. Sci. 361, 931–950.

Henry, D.G., Jarvis, I., Gillmore, G., Stephenson, M., 2019. Raman spectroscopy as a tool to determine the thermal maturity of organic matter: Application to sedimentary, metamorphic and structural geology. Earth Sci. Rev. 198, 102936.

Herman, F., Copeland, P., Avouac, J.-P., Bollinger, L., Mahéo, G., Le Fort, P., Rai, S., Foster, D., Pêcher, A., Stüwe, K., Henry, P., 2010. Exhumation, crustal deformation, and thermal structure of the Nepal Himalaya derived from the inversion of thermochronological and thermobarometric data and modeling of the topography. J. Geophys. Res. 115, B06407.

Hirono, T., Maekawa, Y., Yabuta, H., 2015. Investigation of the records of earthquake slip in carbonaceous materials from the Taiwan Chelungpu fault by means of infrared and Raman spectroscopies. Geochem. Geophys. Geosyst. 16, 2014GC005622.

Hoefs, J., Frey, M., 1976. The isotopic composition of carbonaceous matter in a metamorphic profile from the Swiss Alps. Geochim. Cosmochim. Acta 40, 945–951.

Ishida, T., 1969. Petrography and structure of the area between the Dudh Kosi and the Tamba Kosi, east Nepal. J. Geol. Soc. Japan 75, 115–125.

Itaya, T., 1981. Carbonaceous material in pelitic schists of the Sanbagawa metamorphic belt in central Shikoku, Japan. Lithos 14, 215–224.

Jessup, M.J., Cottle, J.M., Searle, M.P., Law, R.D., Newell, D.L., Tracy, R.J., Waters, D.J., 2008. P-T-t-D paths of Everest Series schist, Nepal. J. Metamorph. Geol. 26, 717–739.

Kelemen, P.B., Manning, C.E., 2015. Reevaluating carbon fluxes in subduction zones, what goes down, mostly comes up. Proc. Natl. Acad. Sci. U.S.A. 112, E3997–E4006.

Khanal, G.P., Wang, J.-M., Wu, F.-Y., Wang, J.-G., Yang, L., 2020. In-sequence buoyancy extrusion of the Himalayan Metamorphic Core, central Nepal: Constraints from monazite petrochronology and thermobarometry. J. Asian. Earth Sci. 199, 104406.

Kiran, S., Satish-Kumar, M., Nakamura, Y., Hokada, T., 2022. Comparison between Raman spectra of carbonaceous material and carbon isotope thermometries in low-medium grade meta-carbonates: Implications for estimation of metamorphic temperature condition. Precambrian Res. 374, 106656.

Kirilova, M., Toy, V.G., Timms, N., Halfpenny, A., Menzies, C., Craw, D., Beyssac, O., Sutherland, R., Townend, J., Boulton, C., Carpenter, B.M., Cooper, A., Grieve, J., Little, T., Morales, L., Morgan, C., Mori, H., Sauer, K.M., Schleicher, A.M., Williams, J., Craw, L., 2018. Textural changes of graphitic carbon by

tectonic and hydrothermal processes in an active plate boundary fault zone, Alpine Fault, New Zealand. Geol. Soc. Spec. Publ. 453, 205–223.

Kohn, M.J., 2008. P-T-t data from central Nepal support critical taper and repudiate large-scale channel flow of the Greater Himalayan Sequence. Geol. Soc. Am. Bull. 120, 259–273.

Kohn, M.J., Wieland, M.S., Parkinson, C.D., Upreti, B.N., 2005. Five generations of monazite in Langtang gneisses: implications for chronology of the Himalayan metamorphic core. J. Metamorph. Geol. 23, 399–406.

Kohn, M.J., Paul, S.K., Corrie, S.L., 2010. The lower Lesser Himalayan sequence: A Paleoproterozoic arc on the northern margin of the Indian plate. Geol. Soc. Am. Bull. 122, 323–335.

Könitzer, S.F., Leng, M.J., Davies, S.J., Stephenson, M.H., 2012. An assessment of geochemical preparation methods prior to organic carbon concentration and carbon isotope ratio analyses of fine-grained sedimentary rocks. Geochemistry Geophys. Geosystems 13, Q0AI02.

Kouketsu, Y., Mizukami, T., Mori, H., Endo, S., Aoya, M., Hara, H., Nakamura, D., Wallis, S., 2014. A new approach to develop the Raman carbonaceous material geothermometer for low-grade metamorphism using peak width. Island Arc 23, 33–50.

Kříbek, B., Sýkorová, I., Machovič, V., Laufek, F., 2008. Graphitization of organic matter and fluid-deposited graphite in Palaeoproterozoic (Birimian) black shales of the Kaya-Goren greenstone belt (Burkina Faso, West Africa). J. Metamorph. Geol. 26, 937–958.

Landis, C.A., 1971. Graphitization of dispersed carbonaceous material in metamorphic rocks. Contrib. Mineral. Petrol. 30, 34–45.

Large, D.J., Christy, A.G., Fallick, A.E., 1994. Poorly crystalline carbonaceous matter in high grade metasediments: implications for graphitization and metamorphic fluid compositions. Contrib. Mineral. Petrol. 116, 108–116.

Larson, K.P., 2012. The geology of the Tama Kosi and Rolwaling valley region, East-Central Nepal. Geosphere 8, 507–517.

Le Fort, P., 1975. Himalayas: the collided range, present knowledge of the continental arc. Am. J. Sci., 275A, 1–44.

Lemonnier, C., Marquis, G., Perrier, F., Avouac, J.-P., Chitrakar, G., Kafle, B., Sapkota, S., Gautam, U., Tiwari, D., Bano, M., 1999. Electrical structure of the Himalaya of central Nepal: High conductivity around the mid-crustal ramp along the MHT. Geophys. Res. Lett. 26, 3261–3264.

Li, Y., Satish-Kumar, M., Kiran, S., Wan, C., Zheng, J., 2022. 2.0 Ga orogenic graphite deposits and associated ^{13}C-enriched meta-carbonate rocks from South China Craton: Implications for global Lomagundi event. Geosci. Front. 13, 101409.

Long, S.P., Gordon, S.M., Young, J.P., Soignard, E., 2016. Temperature and strain gradients through Lesser Himalayan rocks and across the Main Central thrust, south central Bhutan: Implications for transport-parallel stretching and inverted metamorphism. Tectonics 35 (8), 1863–1891.

Long, S.P., Robinson, D.M., 2021. Construction of the Lesser Himalayan–Subhimalayan thrust belt: The primary driver of thickening, exhumation, and high elevations in the Himalayan orogen since the middle Miocene. Geology 49, 1283–1288.

Lünsdorf, N.K., Dunkl, I., Schmidt, B.C., Rantitsch, G., von Eynatten, H., 2014. Towards a higher comparability of geothermometric data obtained by Raman spectroscopy of carbonaceous material. Part I: Evaluation of biasing factors. Geostand. Geoanal. Res. 38, 73–94.

Manoel, T.N., Dexheimer Leite, J.A., 2018. On the origin of the Neoproterozoic Peresopolis graphite deposit, Paraguay Belt, Brazil. J. South Am. Earth Sci. 84, 104–112.

Martín-Méndez, I., Boixereu, E., Villaseca, C., 2016. Mineralogical and isotopic characterization of graphite deposits from the Anatectic Complex of Toledo, central Spain. Miner. Depos. 51, 575–590.

Mathew, G., De Sarkar, S., Pande, K., Dutta, S., Ali, S., Rai, A., Netrawali, S., 2013. Thermal metamorphism of the Arunachal Himalaya, India: Raman thermometry and thermochronological constraints on the tectono-thermal evolution. Int. J. Earth Sci. 102, 1911–1936.

Mathez, E.A., Fogel, R.A., Hutcheon, I.D., Marshintsev, V.K. 1995. Carbon isotopic composition and origin of SiC from kimberlites of Yakutia, Russia. Geochim. Cosmochim. Acta, 59, 781-791.

Menzies, C.D., Wright, S.L., Craw, D., James, R.H., Alt, J.C., Cox, S.C., Pitcairn, I.K., Teagle, D.A.H., 2018. Carbon dioxide generation and drawdown during active orogenesis of siliciclastic rocks in the Southern Alps, New Zealand. Earth Planet. Sci. Lett. 481, 305–315.

Midwood, A.J., Boutton, T.W. 1998. Soil carbonate decomposition by acid has little effect on $\delta^{13}C$ of organic matter. Soil Biol. Biochem. 30, 1301–1307.

Miyashiro, A., 1964. Oxidation and reduction in the Earth's crust with special reference to the role of graphite. Geochim. Cosmochim. Acta 28, 717–729.

Morikiyo, T., 1984. Carbon isotopic study on coexisting calcite and graphite in the Ryoke metamorphic rocks, northern Kiso district, central Japan. Contrib. Mineral. Petrol. 87, 251–259.

Morikiyo, T., 1986. Hydrogen and carbon isotope studies on the graphite-bearing metapelites in the northern Kiso district of central Japan. Contrib. Mineral. Petrol. 94, 165–177.

Muirhead, D.K., Kedar, L., Schito, A., Corrado, S., Bond, C.E., Romano, C., 2021. Raman spectral shifts in naturally faulted rocks. Geochemistry Geophys. Geosystems 22, e2021GC009923.

Müller, R.D., Mather, B., Dutkiewicz, A., Keller, T., Merdith, A., Gonzalez, C.M., Gorczyk, W., Zahirovic, S., 2022. Evolution of Earth's tectonic carbon conveyor belt. Nature 605, 629–639.

Nakamura, Y., Akai, J., 2013. Microstructural evolution of carbonaceous material during graphitization in the Gyoja-yama contact aureole: HRTEM, XRD and Raman spectroscopic study. J. Mineral. Petrol. Sci. 108, 131–143.

Nakamura, Y., Oohashi, K., Toyoshima, T., Satish-Kumar, M., Akai, J., 2015. Strain-induced amorphization of graphite in fault zones of the Hidaka metamorphic belt, Hokkaido, Japan. J. Struct. Geol. 72, 142–161.

Nakamura, Y., Toyoshima, T., Satish-Kumar, M., 2018. Microstructure and geochemical signatures of metasedimentary origin pseudotachylyte: Implications for fluid activity during paleoseismicity. Tectonophysics 745, 170–182.

Nakamura, Y., Yoshino, T., Satish-Kumar, M., 2020. Pressure dependence of graphitization: implications for rapid recrystallization of carbonaceous material in a subduction zone. Contrib. Mineral. Petrol. 175, 32.

Neubeck, A., Broman, C., Ivarsson, M., Holm, N.G., Whitehouse, M., Nilsson, S., Geppert, W., Gervilla, F., 2020. Isotopic signatures of carbon in the 'Los Pobres' graphite mine, Ronda, Spain. J. Petrol. 61, egaa042.

Nover, G., Stoll, J.B., von der Gönna, J., 2005. Promotion of graphite formation by tectonic stress – a laboratory experiment. Geophys. J. Int. 160, 1059–1067.

Oohashi, K., Han, R., Hirose, T., Shimamoto, T., Omura, K., Matsuda, T., 2014. Carbon-forming reactions under a reducing atmosphere during seismic fault slip. Geology 42, 787–790.

Palosaari, J., Latonen, R.-M., Smått, J.-H., Blomqvist, R., Eklund, O., 2016. High-quality flake graphite occurrences in a high-grade metamorphic region in Sortland, Vesterålen, northern Norway. Nor. J. Geol. 96, 19–26.

Parnell, J., Brolly, C., 2021. Increased biomass and carbon burial 2 billion years ago triggered mountain building. Commun. Earth Environ. 2, 238.

Parnell, J., Brolly, C., Boyce, A.J., 2021. Graphite from Palaeoproterozoic enhanced carbon burial, and its metallogenic legacy. Geol. Mag. 158, 1711–1718.

Parrish, R.R., Hodges, K.V., 1996. Isotopic constraints on the age and provenance of the Lesser and Greater Himalayan sequences, Nepalese Himalaya. Geol. Soc. Am. Bull. 108, 904–911.

Pasteris J. D., Wopenka B., 1991. Raman spectra of graphite as indicators of degree of metamorphism. Can. Mineral. 29, 1–9.

Paudel, L.P., 2011. Carbonaceous schists of the Main Central Thrust zone as a source of graphite: a case study from the Kali Gandaki valley, west Nepal. Bull. Department Geol., Nepal 14, 9–14.

Pearson, O.N., DeCelles, P.G., 2005. Structural geology and regional tectonic significance of the Ramgarh thrust, Himalayan fold-thrust belt of Nepal. Tectonics 24, TC4008.

Plank, T., Manning, C.E. 2019. Subducting carbon. Nature 574, 343-352.

Rahl, J., Anderson, K., Brandon, M., Fassoulas, C., 2005. Raman spectroscopic carbonaceous material thermometry of low-grade metamorphic rocks: Calibration and application to tectonic exhumation in Crete, Greece. Earth Planet. Sci. Lett. 240, 339–354.

Rana, S., Sharma, R., Kumar, S., 2021. Carbonaceous material in Larji–Rampur window, Himachal Himalaya: Carbon isotope compositions, micro Raman spectroscopy and implications. J. Earth Syst. Sci. 130, 239.

Rapa, G., Groppo, C., Rolfo, F., Petrelli, M., Mosca, P., Perugini, D., 2017. Titanite-bearing calc-silicate rocks constrain timing, duration and magnitude of metamorphic CO_2 degassing in the Himalayan belt. Lithos 292–293, 364–378.

Rapa, G., Mosca, P., Groppo, C., Rolfo, F., 2018. Detection of tectonometamorphic discontinuities within the Himalayan orogen: Structural and petrological constraints from the Rasuwa district, central Nepal Himalaya. J. Asian Earth Sci. 158, 266–286.

Rawat, R., Sharma, R., 2011. Features and characterization of graphite in Almora Crystallines and their implication for the graphite formation in Lesser Himalaya, India. J. Asian Earth Sci. 42, 51–64.

Robinson, G.R., Jr., Hammarstrom, J.M., Olson, D.W., 2017. Graphite. Chap. J of Schulz, K.J., DeYoung, J.H., Jr., Seal, R.R., II, and Bradley, D.C., eds., Critical mineral resources of the United States—Economic and environmental geology and prospects for future supply. U.S. Geological Survey Professional Paper 1802, p. J1– J24.

Robinson, D.M., DeCelles, P.G., Copeland, P., 2006. Tectonic evolution of the Himalayan thrust belt in western Nepal: Implications for channel flow models. Geol. Soc. Am. Bull. 118, 865–885.

Rodas, M., Luque, F.J., Barrenechea, J.F., Fernández-Caliani, J.C., Miras, A., Fernández-Rodríguez, C., 2000. Graphite occurrences in the low-pressure/high-temperature metamorphic belt of the Sierra de Aracena (southern Iberian Massif). Mineral. Mag. 64, 801–814.

Rouzaud, J.N., Oberlin, A., Beny-Bassez, C., 1983. Carbon films: Structure and microtexture (optical and electron microscopy, Raman spectroscopy). Thin Solid Films 105, 75–96.

Sanyal, P., Acharya, B.C., Bhattacharya, S.K., Sarkar, A., Agrawal, S., Bera, M.K., 2009. Origin of graphite, and temperature of metamorphism in Precambrian Eastern Ghats Mobile Belt, Orissa, India: A carbon isotope approach. J. Asian Earth Sci. 36, 252–260.

Satish-Kumar, M., Wada, H., Santosh, M., 2002. Constraints on the application of carbon isotope thermometry in high- to ultrahigh-temperature metamorphic terranes. J. Metamorph. Geol. 20, 335–350.

Satish-Kumar, M., Jaszczak, J.A., Hamamatsu, T., Wada, H., 2011. Relationship between structure, morphology, and carbon isotopic composition of graphite in marbles: Implications for calcite-graphite carbon isotope thermometry. Am. Mineral. 96, 470–485.

Schubert, C. J., Nielsen, B. 2000. Effects of decarbonation treatments on $\delta^{13}C$ values in marine sediments. Mar. Chem., 72, 55-59.

Searle, M.P., Law, R.D., Godin, L., Larson, K.P., Streule, M.J., Cottle, J.M., Jessup, M.J., 2008. Defining the Himalayan Main Central Thrust in Nepal. J. Geol. Soc. London 165, 523–534.

Sharma, R., Rawat, R., Law, R. 2011. Carbon isotopic evidence for the origin of Himalayan graphite from Almora crystallines. Curr. Sci., 1216–1220.

Shrestha, S., Larson, K.P., Guilmette, C., Smit, M.A., 2017. The P-T-t evolution of the exhumed Himalayan metamorphic core in the Likhu Khola region, East Central Nepal. J. Metamorph. Geol. 35, 663–693.

Skrzypek, E., 2021. First- and second-order Raman spectra of carbonaceous material through successive contact and regional metamorphic events (Ryoke belt, SW Japan). Lithos 388–389, 106029.

Stöcklin, J., 1980. Geology of Nepal and its regional frame: Thirty-third William Smith Lecture. J. Geol. Soc. London 137, 1–34.

Takagi, H., Arita, K., Sawaguchi, T., Kobayashi, K., Awaji, D., 2003. Kinematic history of the Main Central Thrust zone in the Langtang area, Nepal. Tectonophysics 366, 151–163.

Tamang, S., 2022. Along-strike variations of metamorphic CO_2 outputs from the Nepal Himalaya: Comparison between past production and present emissions. PhD thesis. Università degli Studi di Torino, Italy and Université Paris Cité, France (cotutelle), 210 p.

Tamang, S., Groppo, C., Girault, F., Rolfo, F., 2023. Implications of garnet nucleation overstepping for the P–T evolution of the Lesser Himalayan Sequence of central Nepal. J. Metamorph. Geol. 41, 271–297.

Taner, M.F., Drever, C., Yakymchuk, C., Longstaffe, F.J., 2017. Origin of graphite in the Southwestern Grenville Province. Can. Mineral. 55, 1041–1055.

Tuinstra F., Koenig J. L., 1970. Raman spectrum of graphite. J. Chem. Phys. 53, 1126–1130.

Umeda, H., Enami, M., 2014. Testing for robustness on estimation of graphitization degree by Raman spectroscopy. J. Mineral. Petrol. Sci. 109, 279–285.

Unsworth, M.J., Jones, A.G., Wei, W., Marquis, G., Gokarn, S.G., Spratt, J.E., 2005. Crustal rheology of the Himalaya and Southern Tibet inferred from magnetotelluric data. Nature 438, 78–81.

Upreti, B.N., 1999. An overview of the stratigraphy and tectonics of the Nepal Himalaya. J. Asian Earth Sci. 17, 577–606. Pasteris J. D., Wopenka

Valley, J. W., O'Neil, J. R., 1981. $^{13}C/^{12}C$ exchange between calcite and graphite: A possible thermometer in Grenville marbles. Geochim. Cosmochim. Acta, 45, 411–419.

Wada, H., Tomita, T., Matsuura, K., Tuchi, K., Ito, M., Morikiyo, T., 1994. Graphitization of carbonaceous matter during metamorphism with references to carbonate and pelitic rocks of contact and regional metamorphisms, Japan. Contrib. Mineral. Petrol. 118, 217–228.

Wang, G.-F., 1989. Carbonaceous material in the Ryoke metamorphic rocks, Kinki district, Japan. Lithos 22, 305–316.

Wang, J., Liu, J., Zhang, H., Zhang, H., Li, Y., 2020. Metamorphism, geochemistry, and carbon source on sedimentary-metamorphic graphite deposits in eastern Shandong, China. Geol. J., 55, 3748–3769.

Wang, J., Wu, F., Zhang, J., Khanal, G., Yang, L., 2022. The Himalayan collisional orogeny: A metamorphic perspective. Acta Geol. Sin.-Engl. 96, 1842–1866.

Wang, J., Zhang, J., Wei, C., Rai, S., Wang, M., Qian, J., 2015. Characterising the metamorphic discontinuity across the Main Central Thrust Zone of eastern-central Nepal. J. Asian Earth Sci. 101, 83–100.

Webb, A.A.G., Yin, A., Harrison, T.M., Célérier, J., Burgess, W.P., 2007. The leading edge of the Greater Himalayan Crystalline complex revealed in the NW Indian Himalaya: Implications for the evolution of the Himalayan orogen. Geology 35, 955–958.

Whitney, D.L., Evans, B.W., 2010. Abbreviations for names of rock-forming minerals. Am. Mineral. 95, 185–187.

Yakymchuk, C., Godin, L., 2012. Coupled role of deformation and metamorphism in the construction of inverted metamorphic sequences: an example from far-northwest Nepal. J. Metamorph. Geol. 30, 513–535.

Zhu, J., Lui, F., Wang, F., Xu, W., Liu, F., Shi, C., 2021. Carbon isotope and geochemical characteristics of the Paleoproterozoic graphite deposits in the Jiao-Liao-Ji belt, North China Craton: Implications for genesis and depositional environment. Precambrian Res. 362, 106320.

Tables caption

Table 1. Overview of the graphitic phyllites characteristics from the five sites of the Upper Trisuli valley investigated in this study. Statistics of the two high-resolution sampling areas from site A are also given.

Table 2. Overview of carbon content and peak metamorphic temperature from graphitic phyllites in Nepal and in the whole Himalayan orogen. Organized by region, from West to East, data include original values (n=145) and entries from the literature (n=36).

Figures caption

Figure 1. Geological map of Nepal (a) and of the Upper Trisuli valley (b) showing location of the five sampling sites within the graphitic mica-schist unit in the Lesser Himalayan Sequence. (c-g) Small pictures showing the five outcrops studied in the Upper Trisuli valley. Geological information is compiled from several studies (see Amatya and Jnawali, 1994; Upreti, 1999; Girault et al., 2012 and reference herein; Dhital et al., 2015; Rapa et al., 2018; Khanal et al., 2020, Girault et al., 2022) and from our own field works. Topography is drawn using the 1 arc-second DEM provided by GMT6 software.

Figure 2. (a) Raw Raman spectra recorded for ten different graphite locations of a graphitic phyllite sample. D1, G and D2 correspond to defect band 1, graphite band and defect band 2, respectively. (b) Raman spectra after baseline correction for the graphitic phyllite sample A28 (site A). (c) Detail of a Raman spectrum showing the various properties that can be calculated to define the bands (see text).

Figure 3. Protocol for the determination of carbon content from graphitic phyllites using a Scanning Electron Microscope (SEM) coupled with the detections of Back-Scattered Electrons (BSE) and Secondary Electrons (SE) for two samples: ME9 sample (site D) (a-c) and A8 sample (site A) (d-f). (a,d) SEM image captured using BSE. (b,e) SEM image captured using SE highlighting carbon locations in green. (c,f) SEM image processed by ImageJ software to estimate the carbon content (in blue) of the considered thin-section area. These images correspond to a thin-section area of the graphitic phyllite samples ME9 and A8. Calculated carbon content of ME9 and A8 gives 3.7±0.2 % and 6.6±0.4 %, respectively.

Figure 4. Photomicrographs of graphitic phyllites: (a) sample A1 containing carbonates showing the interlayering of the other minerals, (b) sample A8 with graphite layers showing homogeneous distribution of minerals and strongly developed foliation. SEM-BSE images of graphitic phyllites: (c) sample C6 showing the carbonates and other associated minerals, (d) sample A8 showing the graphite occurrence as black color. Mineral abbreviations in the photomicrographs are taken from Whitney and Evans (2010).

Figure 5. SEM micrographs of graphite from graphitic phyllites: (a) sample A8 showing flaky crystals, (b) sample C4 showing flaky graphite crystals associated with carbonates, (c) enlarged image of flaky graphite crystals (red rectangle in (b)) and (d) another enlarged image of flaky graphite crystals.

Figure 6. Comparison of the SEM-BSE method with the CHNS analyzer method to determine the carbon content of graphitic mica-schists. A total of 15 samples were analyzed with both techniques. The volumetric carbon content determined using the SEM-BSE method is compared with the mass TOC content determined using the CHNS method calculated as a volumetric fraction (see text). The identity line is shown as black dashed line. The fit is shown as solid red line ($TOC_{CHNS}=0.914TOC_{SEM}+0.218$; $R^2=0.69$).

Figure 7. Results from site A above Pajung village in the Upper Trisuli valley: (a) photograph of a section of the graphitic phyllite outcrop along the road with two photographs of sample locations as insets; (b) from top to bottom, peak-*T* obtained using the three RSCM methods and carbon isotopic composition ($\delta^{13}C$) of bulk samples, TOC and IC contents obtained using the CHNS analyzer method, and full widths at half maximum (FWHM) for the D1, G and D2 bands as a function of the position

along the profile; and (c) schematic geological cross-section of the whole studied outcrop. Results of the high-resolution sampling areas (HR1 and HR2) are shown in Supp. Fig S13.

Figure 8. Results from site B below Pajung village in the Upper Trisuli valley: (a) photograph of the graphitic phyllite outcrop along the road with a photograph of a sample location as inset; and (b) from top to bottom, peak-*T* obtained using the three RSCM methods and $\delta^{13}C$ of bulk samples, TOC and IC contents obtained using the CHNS analyzer method, and FWHM for the D1, G and D2 bands as a function of the position along the profile.

Figure 9. Results from site C near Goljung village in the Upper Trisuli valley: (a) photograph of the graphitic phyllite outcrop along the road with two photographs of sample locations as insets; and (b) from top to bottom, peak-*T* obtained using the three RSCM methods and $\delta^{13}C$ of bulk samples, TOC and IC contents obtained using the CHNS analyzer method, and FWHM for the D1, G and D2 bands as a function of the position along the profile. The grey-colored vertical band represents the gouge of the shear zone.

Figure 10. Results from site D near Sanjen hydropower site in the Upper Trisuli valley: (a) photograph of a section of the graphitic phyllite outcrop along the road with a photograph of a sample location as inset; (b) from top to bottom, peak-*T* obtained using the three RSCM methods and $\delta^{13}C$ of bulk samples, TOC and IC contents obtained using the CHNS analyzer method, and FWHM for the D1, G and D2 bands as a function of the position along the profile; and (c) schematic geological cross-section of the whole studied outcrop.

Figure 11. Results from site E near Paragaon village in the Upper Trisuli valley: (a) photograph of the graphitic phyllite outcrop along the road with two photographs of sample locations as insets; and

(b) from top to bottom, peak-*T* obtained using the three RSCM methods and $\delta^{13}C$ of bulk samples, TOC and IC contents obtained using the CHNS analyzer method, and FWHM for the D1, G and D2 bands as a function of the position along the profile.

Figure 12. Distribution of (a) total organic carbon (TOC) content, (b) total carbon (TC) content, (c) peak metamorphic temperature (peak-*T*) determined using B-RSCM, and (d) bulk carbon isotopic composition ($\delta^{13}C$) of graphitic phyllites from the five sites.

Figure 13. (a) Inorganic carbon (IC) content as a function of total organic carbon (TOC) content, and carbon isotopic composition ($\delta^{13}C$) as a function of (b) IC content, (c) TOC content and (d) total carbon (TC) content for graphitic phyllite samples. Other data available on graphitic phyllites from the Himalaya are also shown (Evans et al., 2003; Rana et al., 2021). In b-d), $\delta^{13}C$ data from bulk samples (*i.e.*, non-decarbonated samples) are plotted. In c-d), $\delta^{13}C$ data from decarbonated samples are shown.

Figure 14. TOC content as a function of peak-*T* of graphitic mica-schists for the five sites of the Upper Trisuli valley. Small colored diamonds show data for each site. Colored diamond represents the arithmetic mean values for each site. The arithmetic mean for all the sites is plotted as a large orange diamond. Box-plots of the TOC content (on the right) and of the peak-*T* (at the top) of graphitic phyllite separately from the five sites and from all the sites in the Upper Trisuli valley. For each site, the black dots show the data, the red diamond and its error bars show the mean and its associated 1-σ uncertainty, respectively, the box and the line within it show the interquartile range (IQR) and the median, respectively, and the small bars show at both ends the minimum/maximum range.

Figure 15. Map of the graphite occurrence in the Nepal Himalayas. The surface area extension of the graphitic mica-schist unit is shown as yellowish colored areas. The collected samples from our study (*n*=145) and from the literature (*n*=36) are shown as green and blue stars, respectively. Regional mean and min/max range of TOC content and inferred peak-*T* are also given.

Figure 16. Distribution of various carbon isotopic composition ($\delta^{13}C$) data from the bulk at different orogenic belts worldwide, including the present study area. The different colors specify the countries. The box and the solid vertical bars represent the min/max range and the $\delta^{13}C$ average at each location. The dashed vertical bar represents the overall mean $\delta^{13}C$ value considering all the data plotted. Data are taken from the literature (Hoefs and Frey, 1976; Morikiyo, 1984, 1986; Baker, 1988; Large et al., 1994; Rodas et al., 2000; Evans et al., 2008; Sanyal et al., 2009; Barrenechea et al., 2009; Sharma et al., 2011; Martin-Méndez et al., 2016; Taner et al., 2017; Manoel and Dexheimer Leite, 2018; Menzies et al., 2018; Wang et al., 2020; Neubeck et al., 2020; Zhu et al., 2021; Rana et al., 2021; Li et al., 2022).

Figure 17. Simplified tectonic cross-section of the Nepal Himalaya showing the graphitic mica-schist unit and the current metamorphic CO_2 emission zones reported at the surface and their proposed sources. The location of the cross-section is shown in Figs. 1 and 15. The locations of current CO_2 emission zones are taken from the literature (Becker et al., 2008; Evans et al., 2008; Craw and Upton, 2014; Girault et al., 2014, 2018, 2022, in press a,b). The isotherms are taken from Wang et al. (2022). MFT: Main Frontal Thrust; MBT: Main Boundary Thrust; RT: Ramgarh Thrust; MCT: Main Central Thrust; STDS: South Tibetan Detachment System.

Table 1

Site	Site A				Site B	Site C	Site D	Site E	All sites (A–E)
	Spacing of 10 m	HR1	HR2	All samples					
Location	Above Pajung village				Below Pajung village	Near Goljung village	Near Sanjen village	Near Paragaon village	Upper Trisuli valley
Coordinates (WGS84)[a]	28.18542°N/ 85.32368°E, 2028 m	28.18507°N/ 85.32302°E, 2018 m	28.18508°N/ 85.32208°E, 2024 m		28.18603°N/ 85.33128°E, 1891 m	28.17973°N/ 85.329[illegible]E, 1629 m	28.21575°N/ 85.28160°E, 2277 m	28.20458°N/ 85.29831°E, 2339 m	
Number of samples	25	11	11	43	6	7	10	10	74[b]
TOC content (%)									
Mean ±1-σ	4.2±0.3	3.8±0.6	2.8±0.2	3.[illegible]±0.2	3.5±0.6	2.5±0.8	3.6±0.3	4.1±0.3	3.7±0.2
Min/max range	2.4/9.0	2.1/6.5	1.9/4.0	1.9/9.0	1.6/5.3	1.0/7.0	1.6/4.8	2.9/5.7	0.9/9.0
Dispersion (%)	37±6	48±13	24±6	41±5	41±14	81±33	27±7	20±5	41±4
TC content (%)									
Mean ±1-σ	5.1±0.6	3.6±0.5	3.0±0.3	4.2±0.4	3.0±0.4	9.0±0.7	3.6±0.4	4.0±0.3	4.5±1.4
Min/max range	2.5/12.6	2.0/6.5	1.8/5.4	1.7±12.6	1.4/4.4	6.2/10.9	1.7/4.7	2.8/5.5	1.4/12.6
Dispersion (%)	55±10	46±12	34±8	56±8	36±12	20±6	31±8	20±5	55±7
FWHM D1 band									

Mean ±1-σ	42.7±0.9	45.8±1.0	43.0±1.1	43.6±0.6	40.5±1.0	40.3±1.7	44.1±0.9	40.3±0.6	42.6±0.5
Min/max range	35.6/54.0	40.9/50.6	39.0/51.7	35.6/54.0	38.24/45.1	35.8/47.5	39.4/48.2	37.3/43.7	35.6/54.0
Dispersion (%)	9.6±0.2	6.9±0.1	8.5±0.2	9.2±0.1	6.1±0.2	11.5±0.5	5.9±0.1	5.1±0.1	9.1±0.1
FWHM G band									
Mean ±1-σ	21.4±0.4	19.7±0.6	20.5±0.2	20.8±0.3	21.0±0.3	20.1±0.8	20.5±0.2	20.6±0.3	20.7±0.2
Min/max range	19.2/28.3	14.8/22.3	19.6/22.0	14.8/28.3	19.8/21.9	19.0/24.6	19.4/21.4	19.6/23.0	14.8/28.3
Dispersion (%)	8.4±0.1	10.8±0.4	3.76±0.04	9.1±0.1	3.9±0.1	10.1±0.4	2.90±0.03	4.7±0.1	7.9±0.1
FWHM D2 band									
Mean ±1-σ	20.6±1.6	18.5±1.5	20.7±1.5	20.3±1.0	16.9±1.7	14.0±1.3	16.6±1.8	13.7±0.7	18.1±0.7
Min/max range	11.3/44.3	10.6/25.0	15.4/30.2	10.6/44.3	11.8/21.7	11.2/21.2	10.8/25.3	10.6/17.2	10.6/44.3
Dispersion (%)	35.6±2.6	27.5±2.3	24.1±1.7	32.2±1.6	24.4±2.4	24.2±2.2	30.7±3.3	15.8±0.8	33.6±1.3
Peak-*T* (°C)									
Mean ±1-σ	549.7±2.5	562.1±4.8	554.6±3.6	554.6±2.5	558.7±6.1	559.1±8.2	565.5±4.2	563.1±2.7	557.7±1.8
Min/max range	518.7/589.9	531.0/587.8	531.4/569.5	518.7/589.9	530.3/574.1	520.9/580.6	541.7/581.1	549.4/575.1	518.7/589.9
Dispersion (%)	2.96±0.02	2.78±0.02	2.18±0.01	2.87±0.01	2.69±0.03	3.90±0.06	2.23±0.02	1.53±0.01	2.79±0.01

[a]The coordinates indicate point 0 along each profile.

[b]Data from the three samples ME1, ME9 and ME15 are presented in Supp. Table S1.

Table 2

Location / Site	Number of samples	TOC content (%)			Peak-*T* (°C)			References
		Mean ±1-σ	Min/max range	Dispersion (%)	Mean ±1-σ	Min/max range	Dispersion (%)	
Far–Western Nepal								
Baitadi-Dharchula	6				514.3±13.5	477.6/546.5	6±2	Beyssac et al. (2004); Bollinger et al. (2004)
	2	1.4±0.3	1.0/1.7	37±21				This study
Jumla-Humla	9	0.8±0.2	0.04/2.0	91±35				This study
Mid-Western Nepal								
Lower Dolpo	4	0.5±0.2	0.2/1.1	94±56				This study
Western Nepal								
Kali Gandaki valley	2	8.9±1.4	7.5/10.3	22±4				Evans et al. (2008)
	8	20.0±1.3	15/25	23±6				Paudel (2012)
	10	3.1±0.5	1.3/5.8	51±14				This study
Myagdi valley	3				530.1±8.5	513.4/540.8	3±1	Beyssac et al. (2004); Bollinger et al. (2004)
Marsyandi valley	12				536.7±3.6	514.7/553.1	2±1	Beyssac et al. (2004); Bollinger et al. (2004)
	3	3.6±1.5	0.7/5.5	71±41				This study
Barpak area	2	6.0±2.0	4.0/8.0	47±28				This study
Central Nepal								
Ruby valley	2	3.0±1.4	1.6/4.5	67±46				This study
Upper Trisuli valley	77	3.6±0.2	0.5/9.0	42±2	557.7±1.8	518.7/589.9	2.79±0.01	This study

Bhote Koshi valley	4				536.3±9.6	513.5/560.7	4±1	Beyssac et al. (2004); Bollinger et al. (2004)
	17	2.9±0.6	0.7/10.4	81±21				This study
Eastern Nepal								
Akhuwatar area	8	3.6±0.4	1.1/5.1	33±9				This study
Leuti area	8	2.3±0.6	0.3/4.6	78±29				This study
Chainpur area	2	0.2±0.1	0.2/0.3	41±23				This study
Himachal Pradesh, India								
Larji-Rampur window	3	1.7±0.3	1.0/2.1	34±7				Rana et al. (2021)

Declaration of interests

☒The authors declare that they have no known competing financial interests or personal relationships that could have appeared to influence the work reported in this paper.

☐The authors declare the following financial interests/personal relationships which may be considered as potential competing interests:

Highlights (≤85 characters)

- Carbon stored as flaky graphite revealed in Nepal in Lesser Himalayan phyllites
- A microscopy method to quantify organic carbon content is developed and validated
- Carbon content and peak temperature from Raman spectroscopy coherent at all scales
- Higher peak metamorphic temperature in Upper Lesser Himalaya of Central Nepal
- Significant organic carbon stored in orogens to consider in global carbon budget

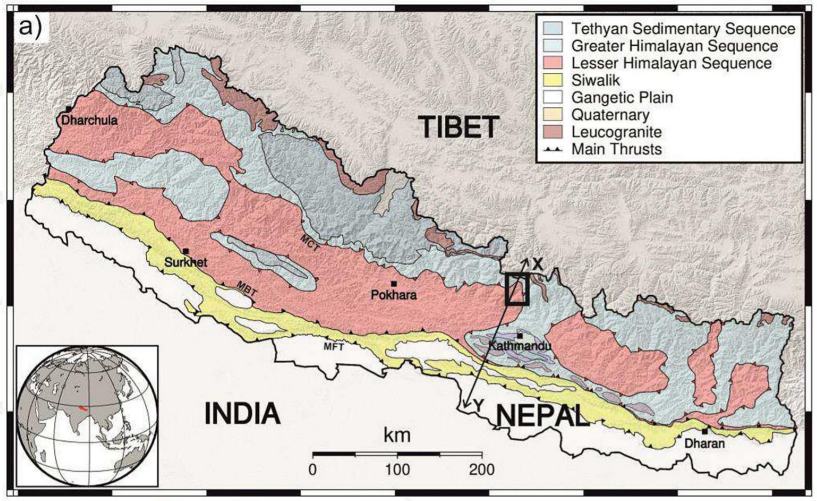
a)
Tethyan Sedimentary Sequence
Greater Himalayan Sequence
Lesser Himalayan Sequence
Siwalik
Gangetic Plain
Quaternary
Leucogranite
Main Thrusts
TIBET
INDIA
NEPAL
Dharchula
Surkhet
Pokhara
Kathmandu
Dharan
MCT
MBT
MFT
X
Y
km
0
100
200
80°
81°
82°
83°
84°
85°
86°
87°
88°
30°
29°
28°
27°

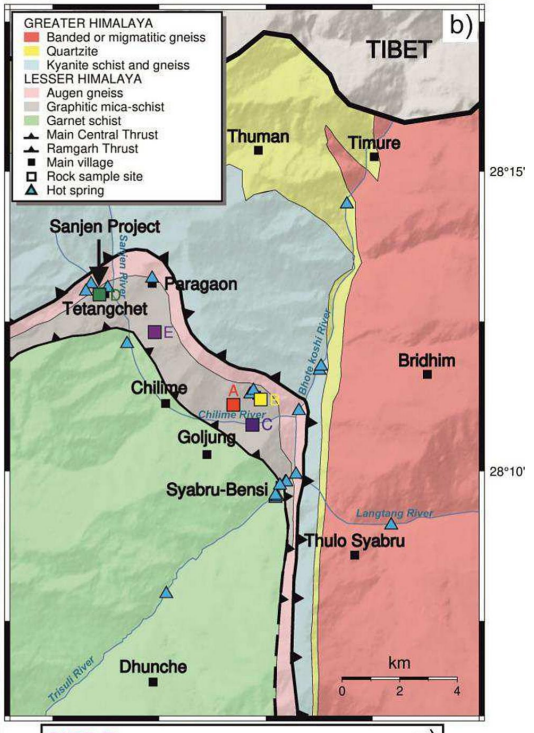
b)
GREATER HIMALAYA
Banded or migmatitic gneiss
Quartzite
Kyanite schist and gneiss
LESSER HIMALAYA
Augen gneiss
Graphitic mica-schist
Garnet schist
Main Central Thrust
Ramgarh Thrust
Main village
Rock sample site
Hot spring
TIBET
Thuman
Timure
Sanjen Project
Sanjen River
Paragaon
Tetangchet
E
Bridhim
Bhote Koshi River
Chilime
A
C
Chilime River
Goljung
Syabru-Bensi
Langtang River
Thulo Syabru
Dhunche
Trisuli River
km
0
2
4
85°16'
85°20'
85°24'
28°15'
28°10'

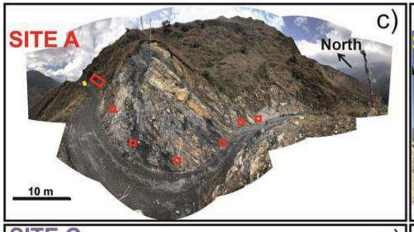
c)
SITE A
North
10 m

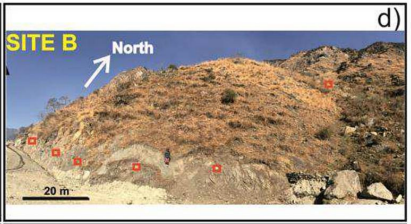
d)
SITE B
North
20 m


SITE C
e)
South
10 m


SITE D
f)
South
10 m


SITE E
g)
North
10 m

Figure 1

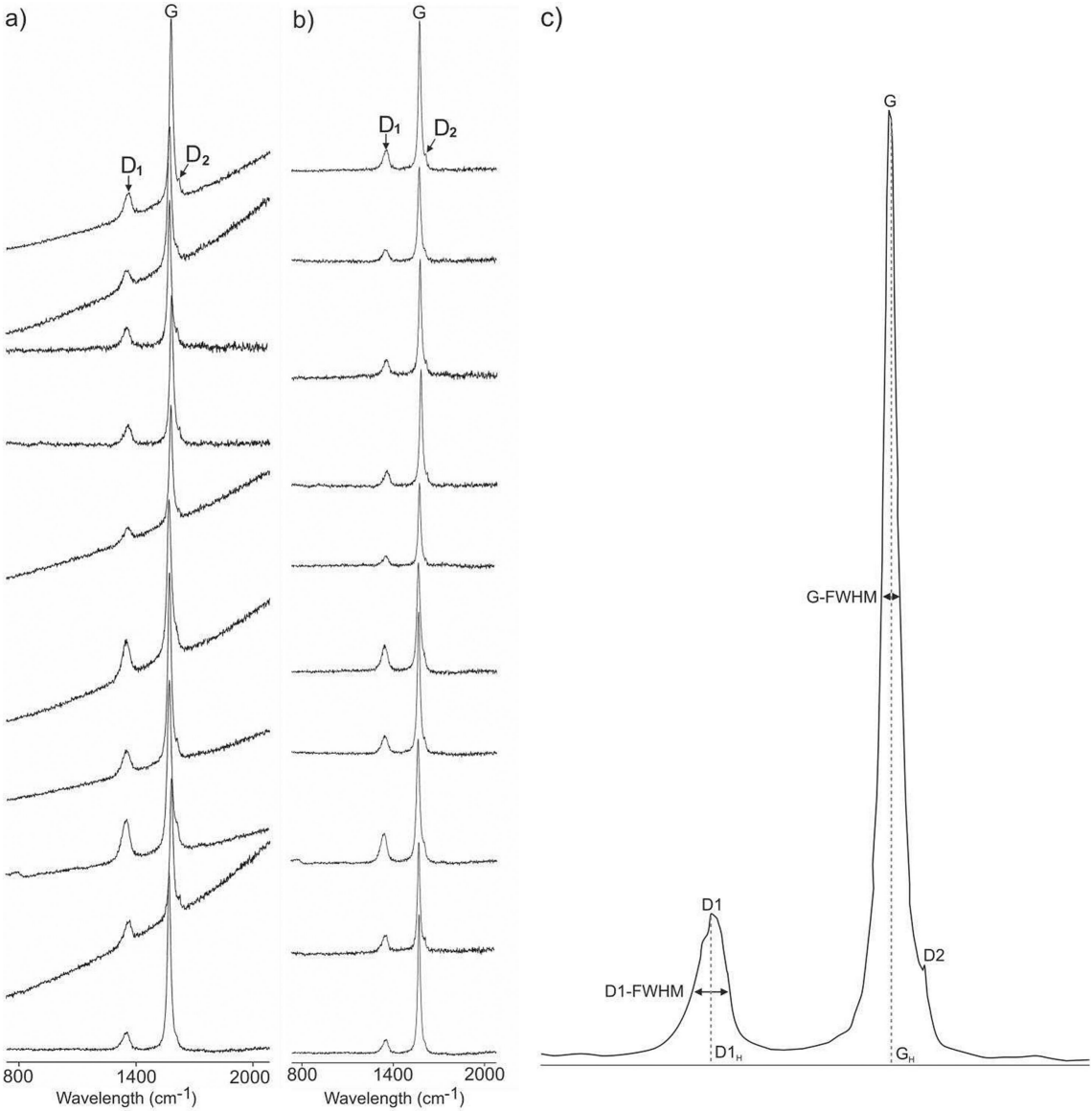
a)
G
D1
D2
800
1400
2000
Wavelength (cm-1)
b)
G
D1
D2
800
1400
2000
Wavelength (cm-1)
c)
G
G-FWHM
D1
D2
D1-FWHM
D1H
GH

Figure 2

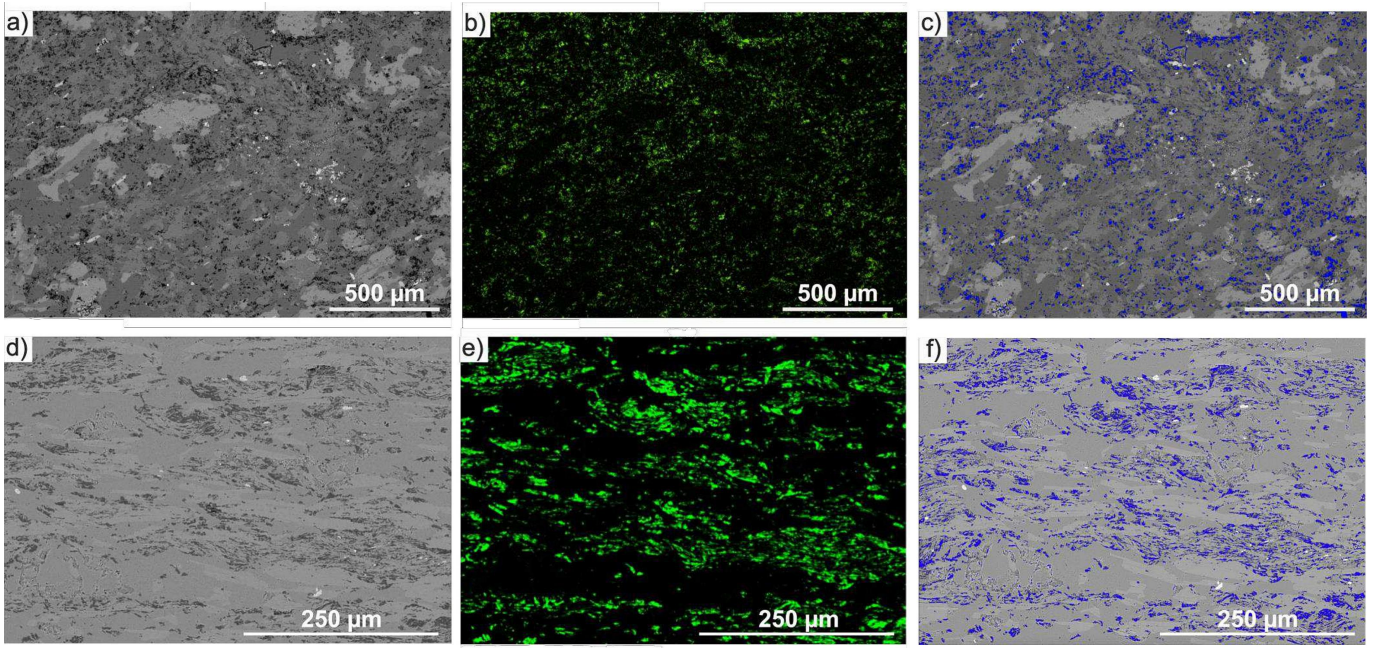

Figure 3

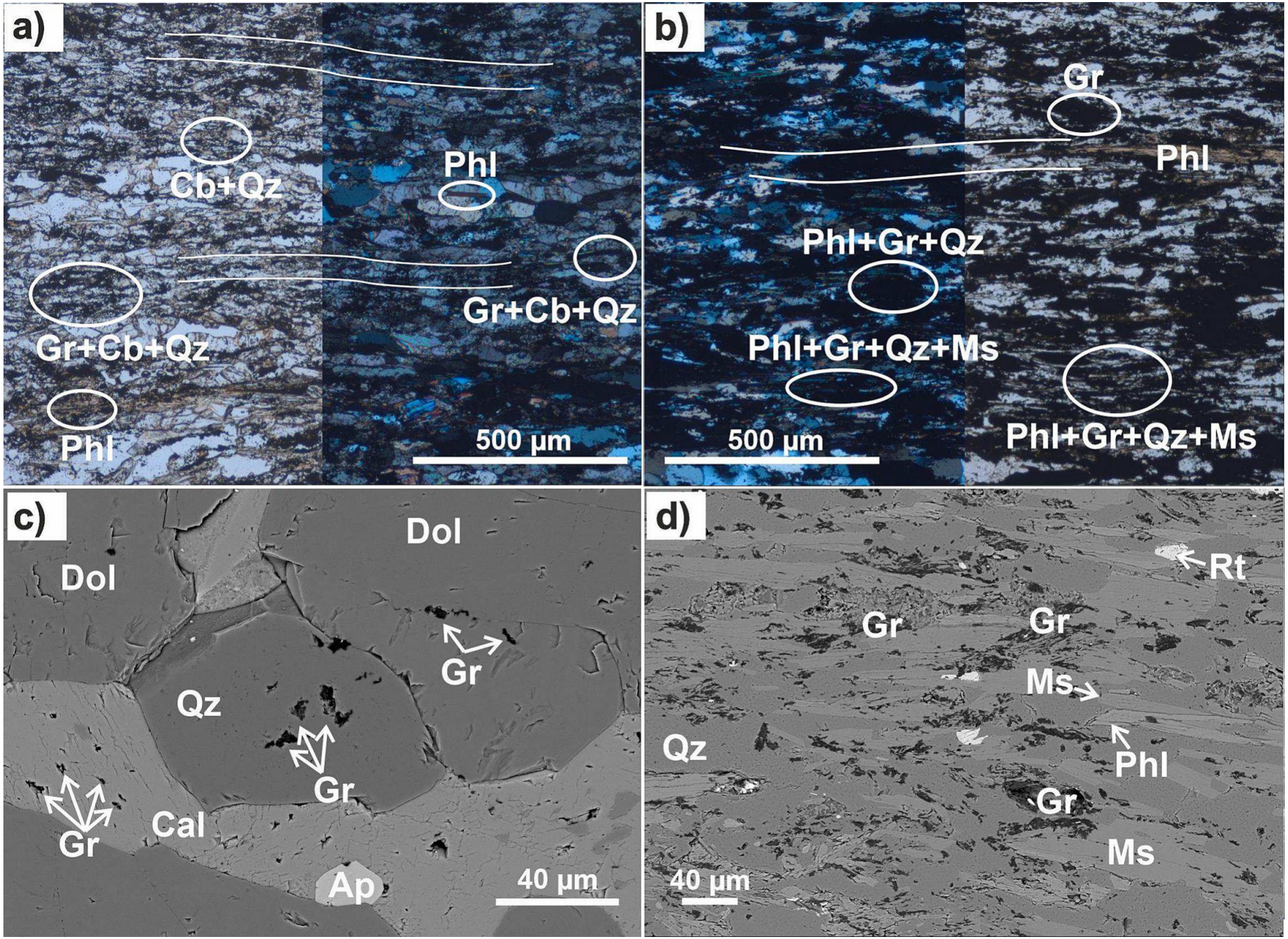
a)
Cb+Qz
Phl
Gr+Cb+Qz
Gr+Cb+Qz
Phl
500 µm
b)
Gr
Phl
Phl+Gr+Qz
Phl+Gr+Qz+Ms
500 µm
Phl+Gr+Qz+Ms
c)
Dol
Dol
Gr
Qz
Gr
Gr
Cal
Ap
40 µm
d)
Rt
Gr
Gr
Ms
Qz
Phl
Gr
Ms
40 µm

Figure 4

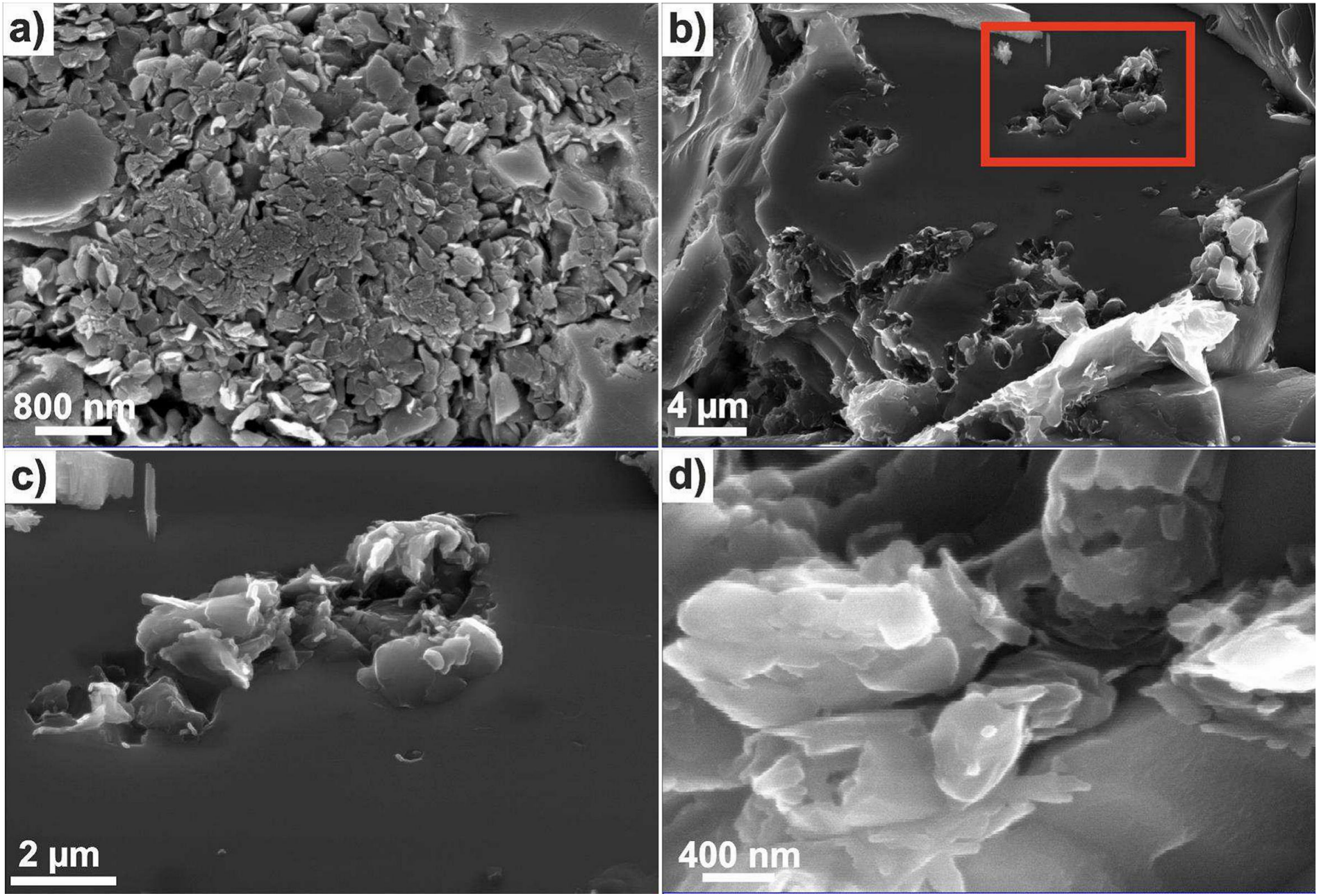

Figure 5

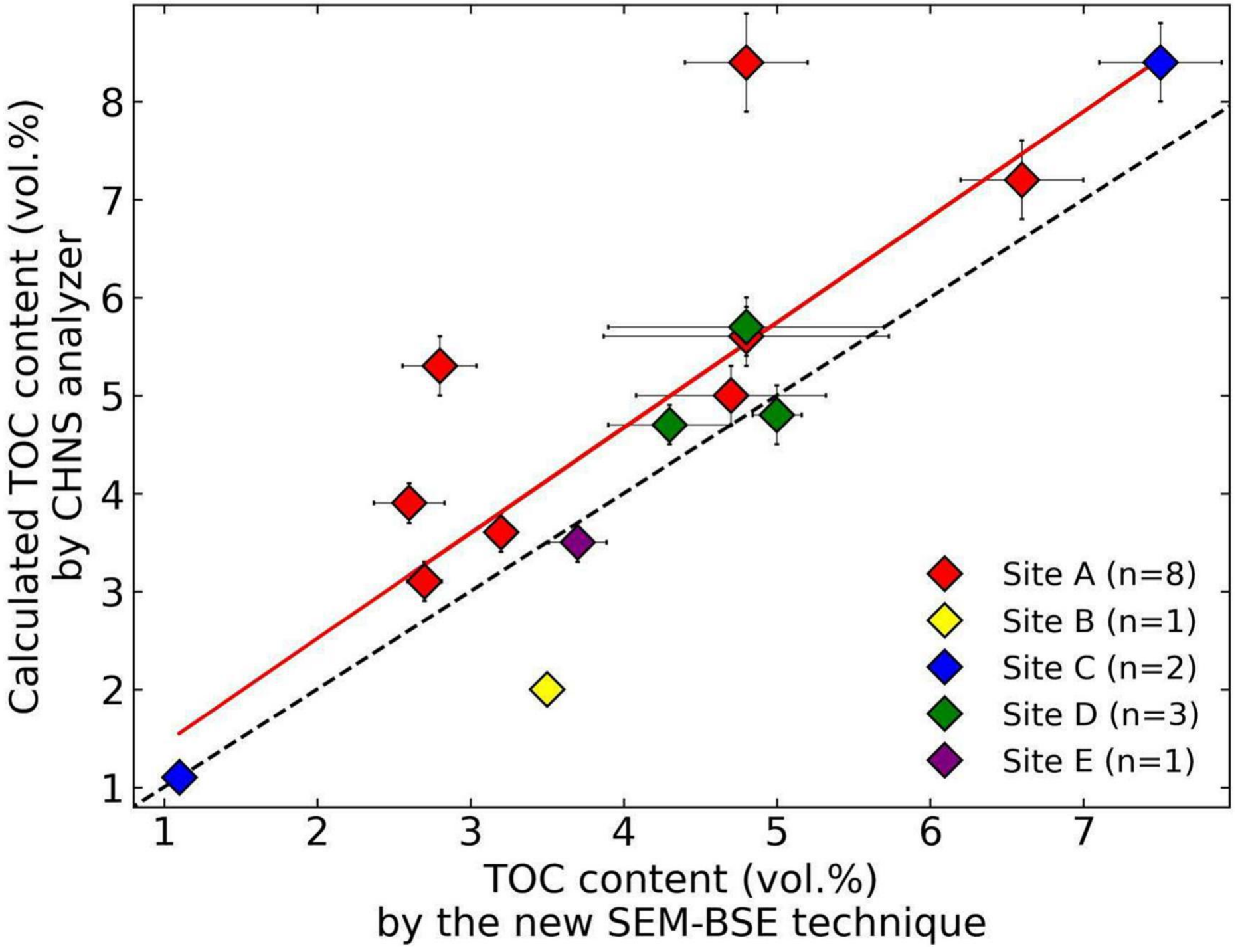
Calculated TOC content (vol.%)
by CHNS analyzer
TOC content (vol.%)
by the new SEM-BSE technique
Site A (n=8)
Site B (n=1)
Site C (n=2)
Site D (n=3)
Site E (n=1)
1
2
3
4
5
6
7
8

Figure 6

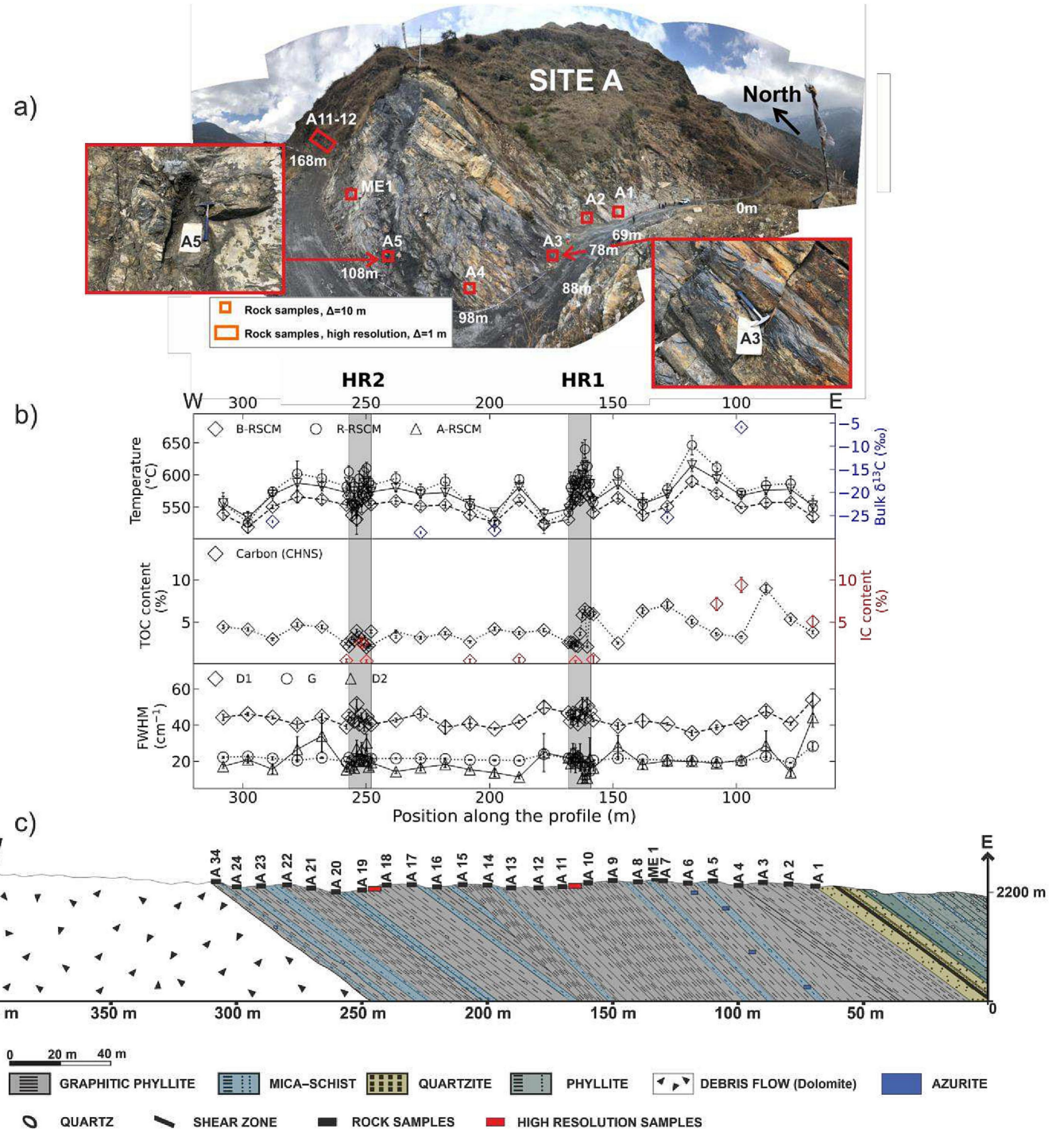
a)
SITE A
North
A11-12
168m
ME1
A2
A1
0m
69m
A3
78m
A5
108m
A4
88m
98m
Rock samples, Δ=10 m
Rock samples, high resolution, Δ=1 m
b)
HR2
HR1
W
E
B-RSCM
R-RSCM
A-RSCM
Temperature (°C)
Bulk δ13C (‰)
Carbon (CHNS)
TOC content (%)
IC content (%)
D1
G
D2
FWHM (cm−1)
Position along the profile (m)
c)
W
E
2200 m
0
400 m
350 m
300 m
250 m
200 m
150 m
100 m
50 m
0 20 m 40 m
GRAPHITIC PHYLLITE
MICA–SCHIST
QUARTZITE
PHYLLITE
DEBRIS FLOW (Dolomite)
AZURITE
QUARTZ
SHEAR ZONE
ROCK SAMPLES
HIGH RESOLUTION SAMPLES

Figure 7

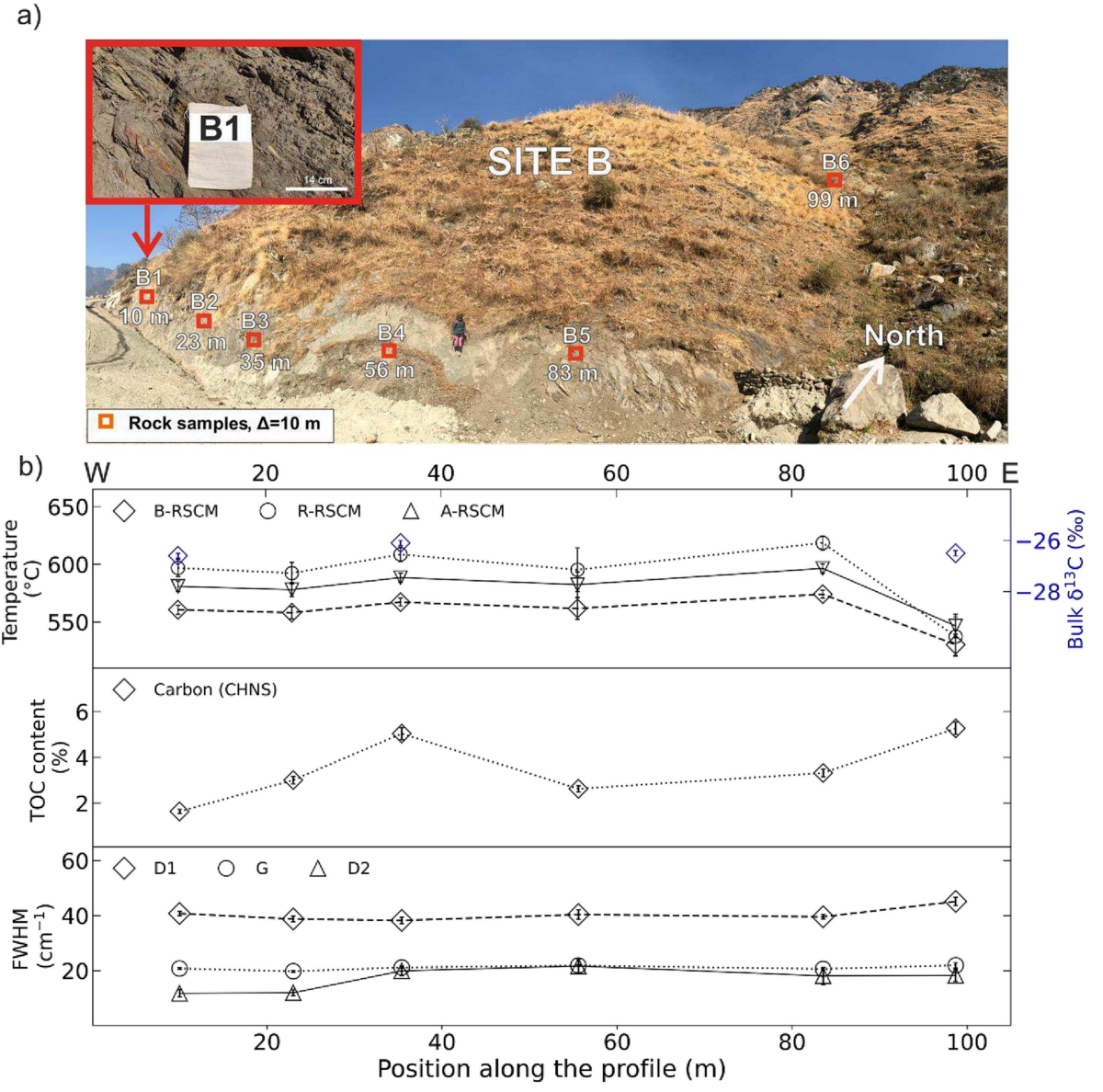
a)
B1
14 cm
SITE B
B6
99 m
B1
10 m
B2
23 m
B3
35 m
B4
56 m
B5
83 m
North
Rock samples, Δ=10 m
b)
W
20
40
60
80
100
E
B-RSCM
R-RSCM
A-RSCM
Temperature (°C)
650
600
550
−26
−28
Bulk δ13C (‰)
Carbon (CHNS)
TOC content (%)
6
4
2
D1
G
D2
FWHM (cm−1)
60
40
20
Position along the profile (m)

Figure 8

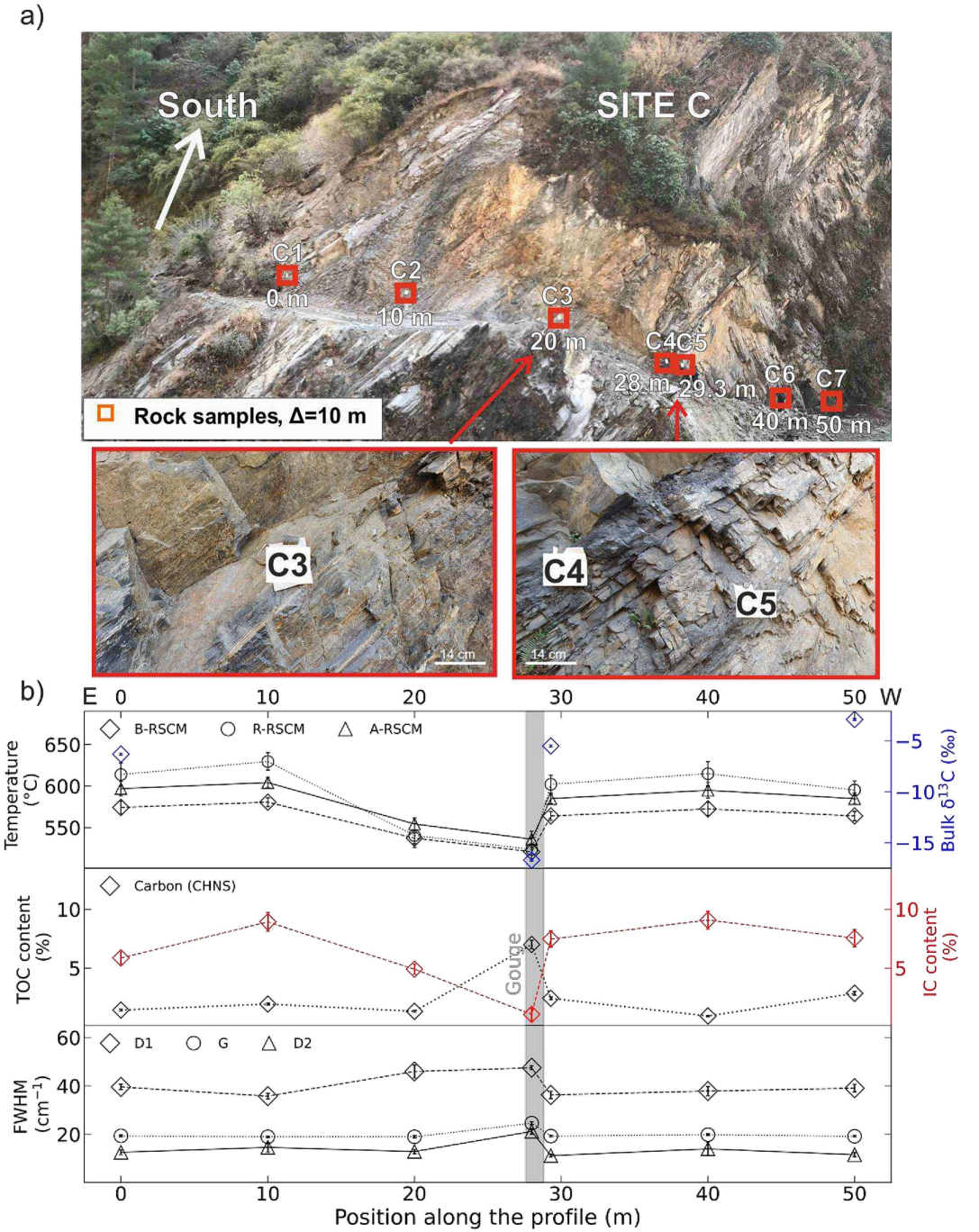
a)
South
SITE C
C1
0 m
C2
10 m
C3
20 m
C4C5
28 m
29.3 m
C6
40 m
C7
50 m
Rock samples, Δ=10 m
C3
14 cm
C4
C5
14 cm
b)
E
0
10
20
30
40
50
W
B-RSCM
R-RSCM
A-RSCM
Temperature (°C)
650
600
550
−5
−10
−15
Bulk δ13C (‰)
Carbon (CHNS)
TOC content (%)
10
5
Gouge
IC content (%)
D1
G
D2
FWHM (cm−1)
60
40
20
Position along the profile (m)

Figure 9

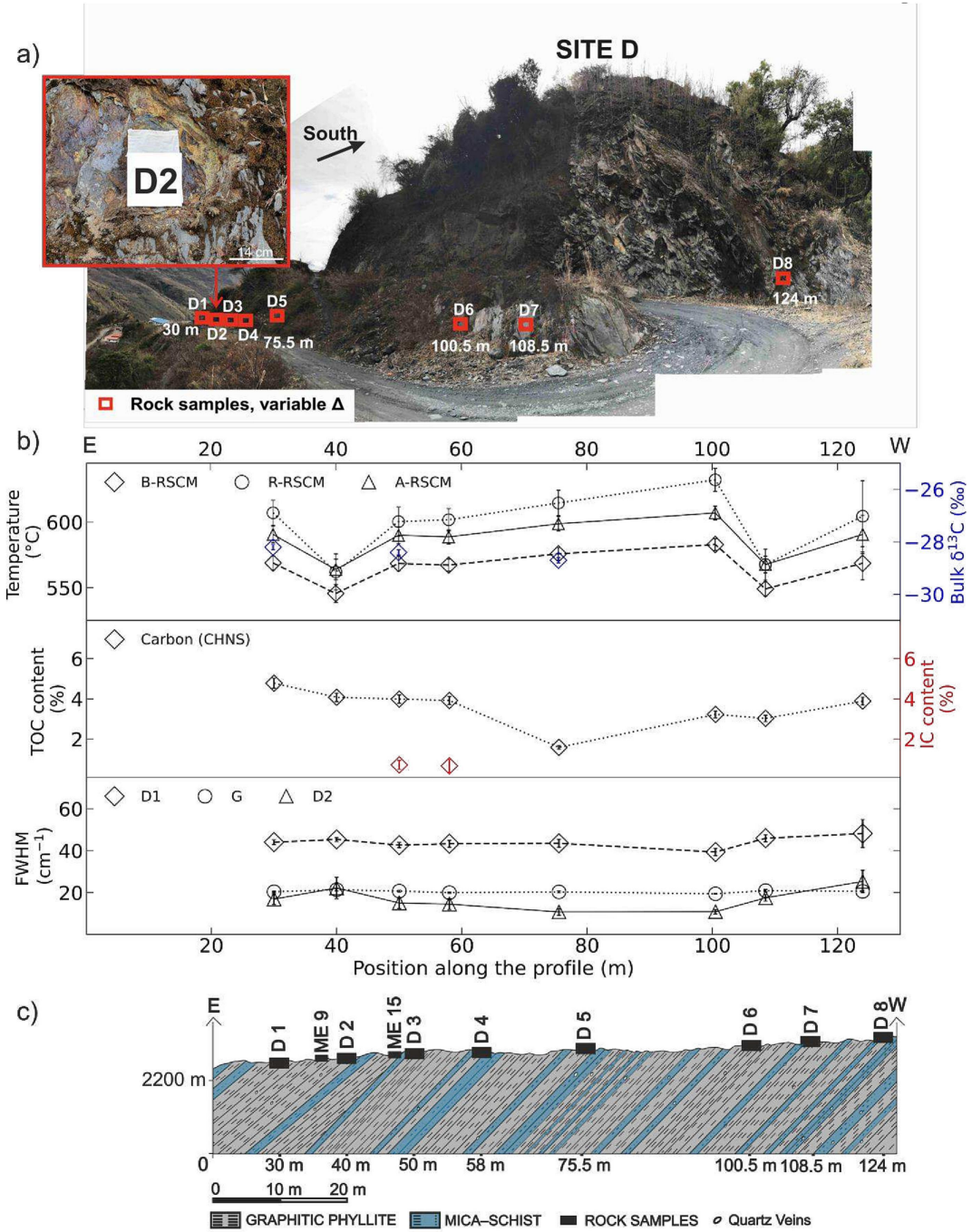
a)
SITE D
D2
14 cm
South
D1
D3
D5
30 m
D2
D4
75.5 m
D6
100.5 m
D7
108.5 m
D8
124 m
Rock samples, variable Δ
b)
E
W
B-RSCM
R-RSCM
A-RSCM
Temperature (°C)
Bulk δ13C (‰)
Carbon (CHNS)
TOC content (%)
IC content (%)
D1
G
D2
FWHM (cm−1)
Position along the profile (m)
c)
E
W
D 1
ME 9
D 2
ME 15
D 3
D 4
D 5
D 6
D 7
D 8
2200 m
0
30 m
40 m
50 m
58 m
75.5 m
100.5 m
108.5 m
124 m
0
10 m
20 m
GRAPHITIC PHYLLITE
MICA–SCHIST
ROCK SAMPLES
Quartz Veins

Figure 10

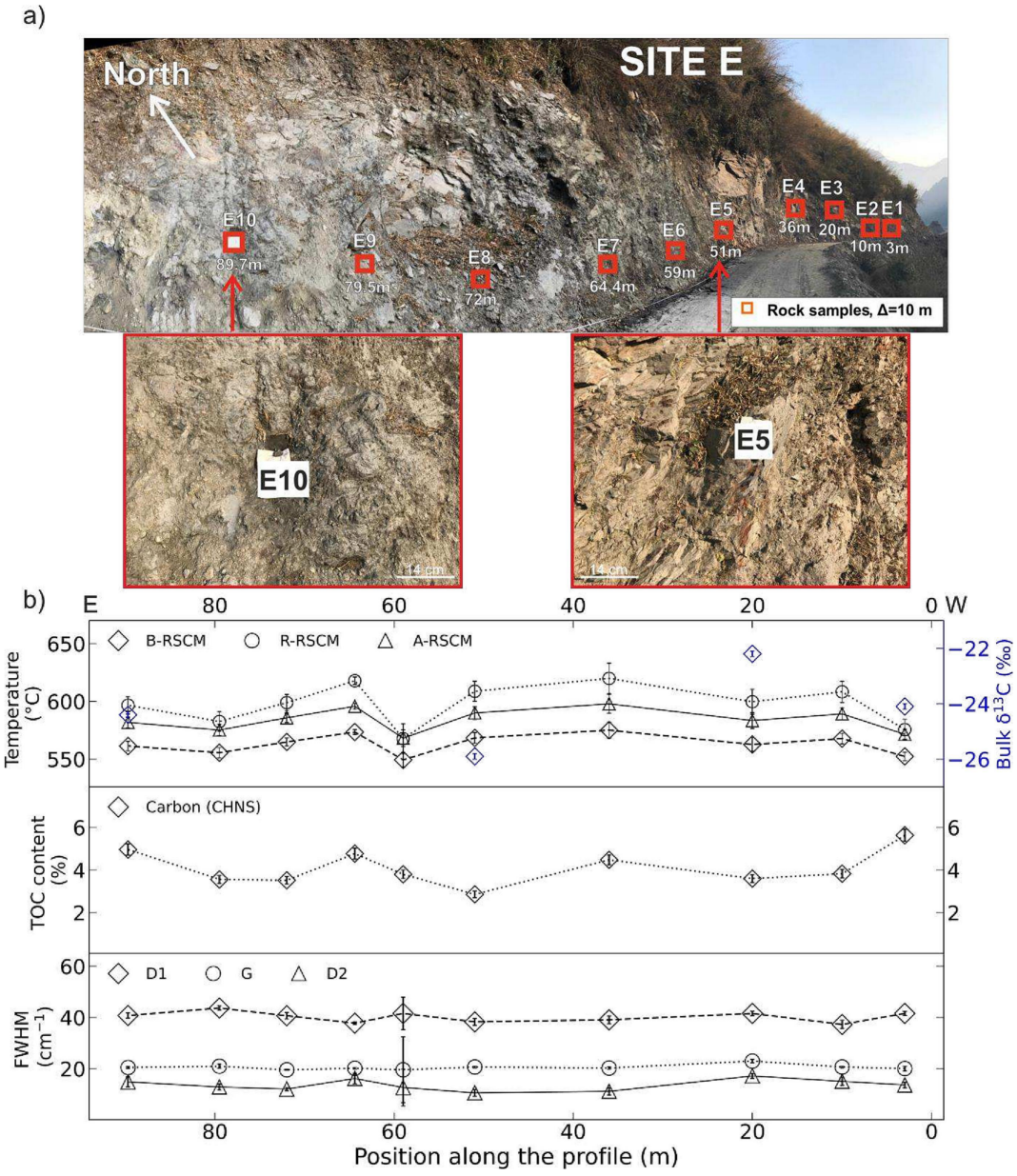
a)
North
SITE E
E10
89.7m
E9
79.5m
E8
72m
E7
64.4m
E6
59m
E5
51m
E4
36m
E3
20m
E2
10m
E1
3m
Rock samples, Δ=10 m
E10
E5
14 cm
14 cm
b)
E
80
60
40
20
0 W
Temperature (°C)
650
600
550
B-RSCM
R-RSCM
A-RSCM
Bulk δ13C (‰)
−22
−24
−26
Carbon (CHNS)
TOC content (%)
6
4
2
D1
G
D2
FWHM (cm−1)
60
40
20
80
60
40
20
0
Position along the profile (m)

Figure 11

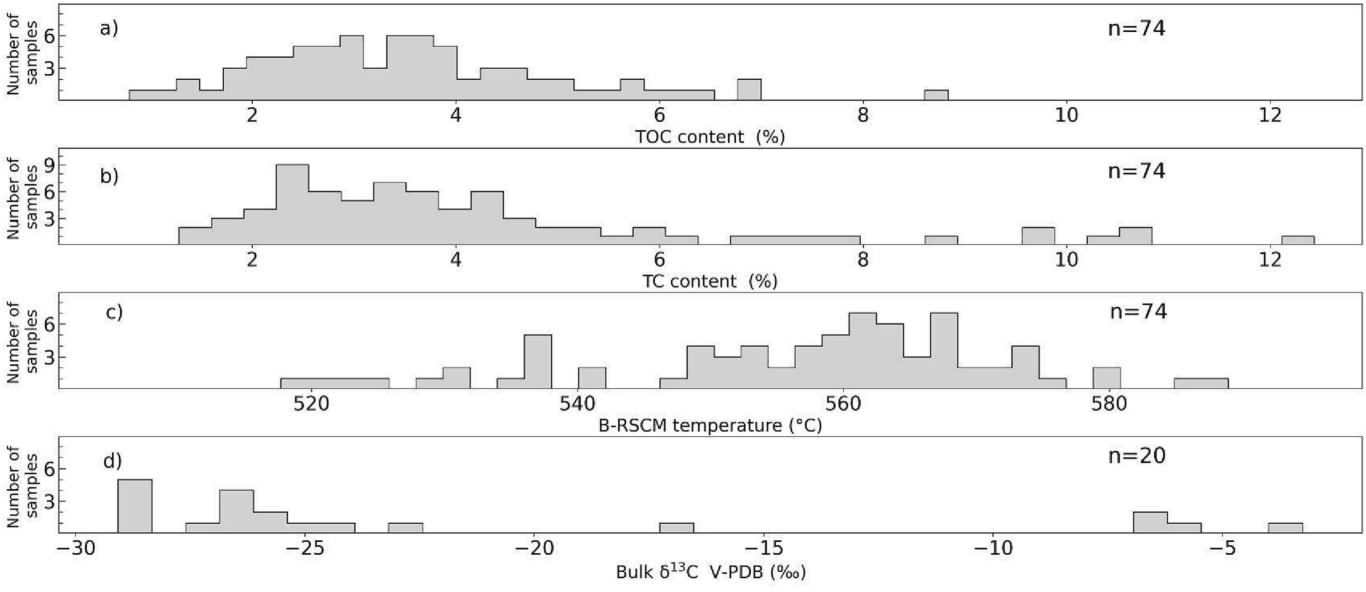
a)
n=74
Number of samples
TOC content (%)
b)
n=74
TC content (%)
c)
n=74
B-RSCM temperature (°C)
d)
n=20
Bulk δ13C V-PDB (‰)

Figure 12

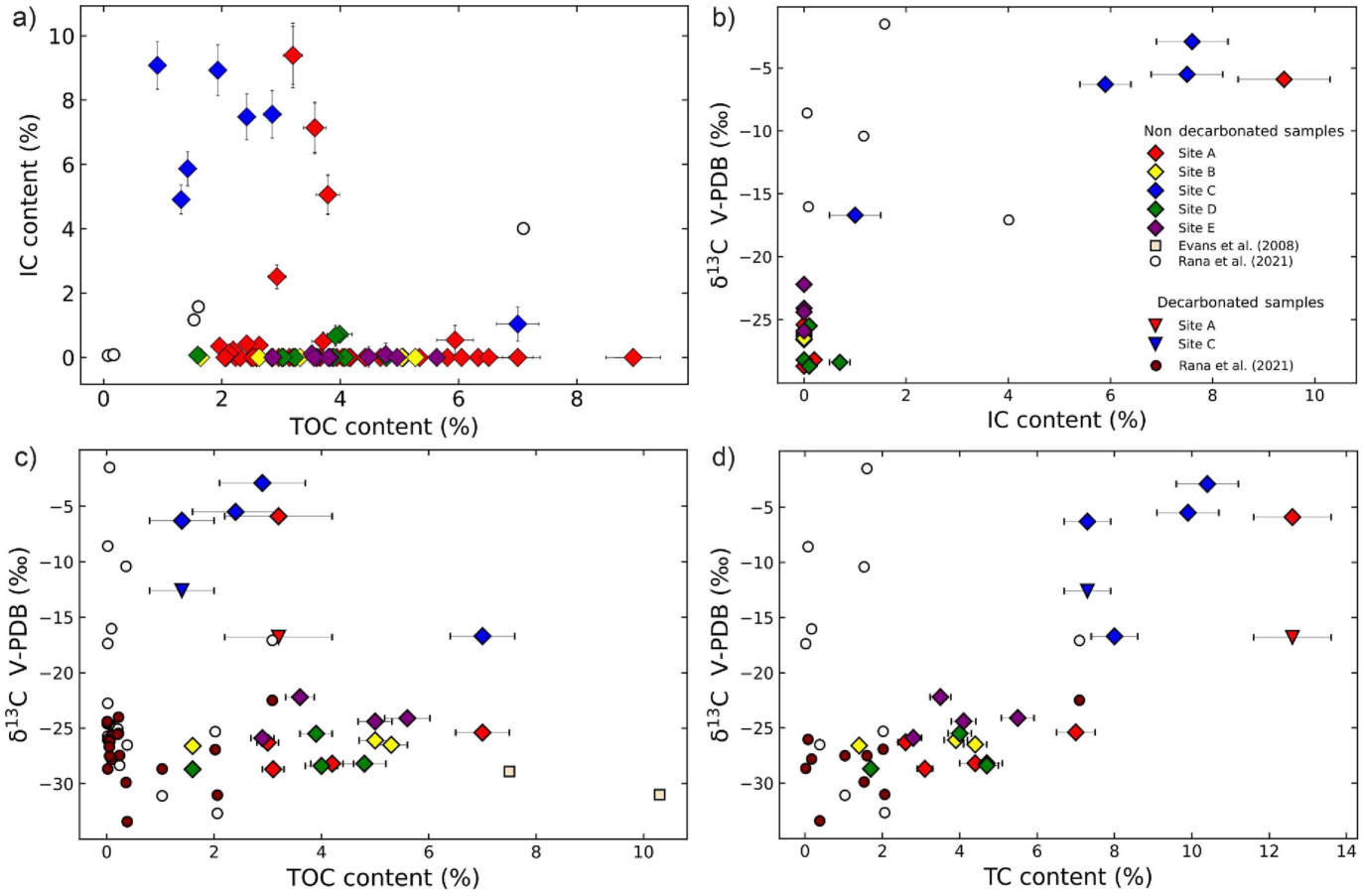
a)
IC content (%)
TOC content (%)
b)
δ13C V-PDB (‰)
IC content (%)
Non decarbonated samples
Site A
Site B
Site C
Site D
Site E
Evans et al. (2008)
Rana et al. (2021)
Decarbonated samples
Site A
Site C
Rana et al. (2021)
c)
δ13C V-PDB (‰)
TOC content (%)
d)
δ13C V-PDB (‰)
TC content (%)

Figure 13

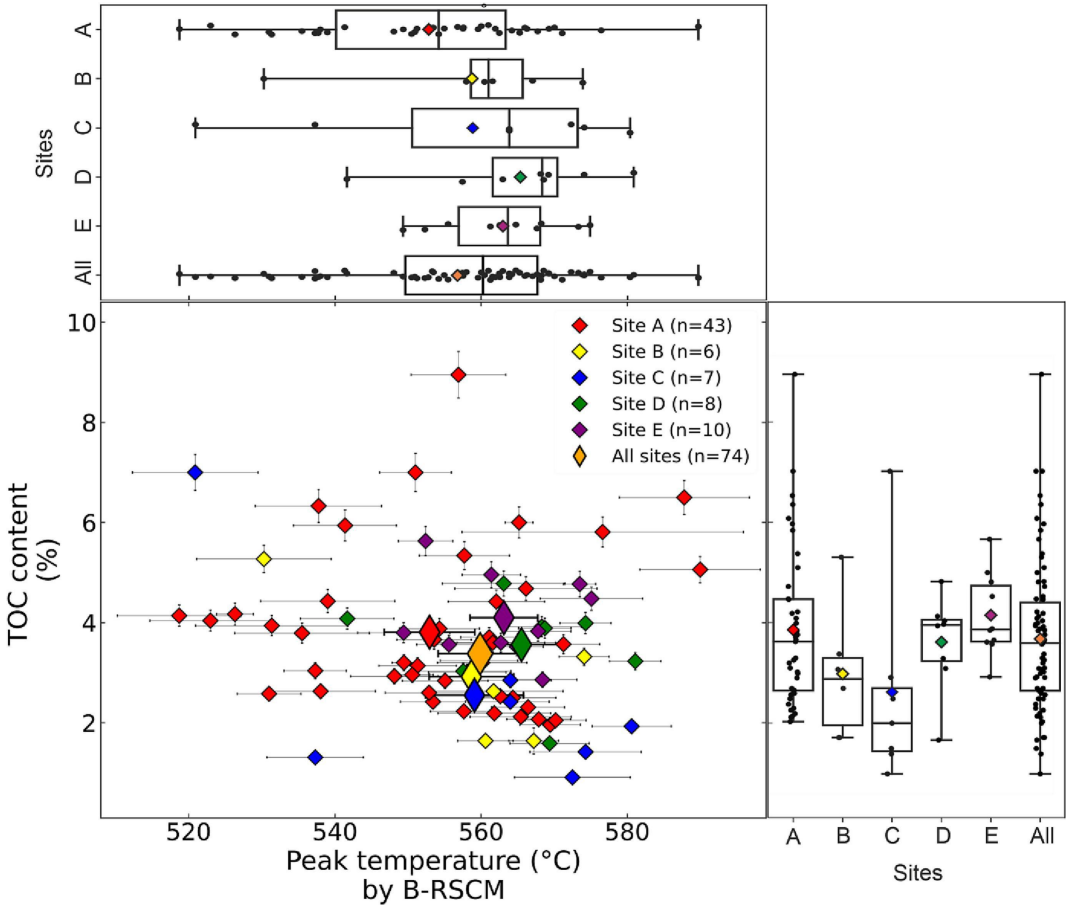
Sites
A
B
C
D
E
All
TOC content (%)
10
8
6
4
2
Site A (n=43)
Site B (n=6)
Site C (n=7)
Site D (n=8)
Site E (n=10)
All sites (n=74)
520
540
560
580
Peak temperature (°C) by B-RSCM
A
B
C
D
E
All
Sites

Figure 14

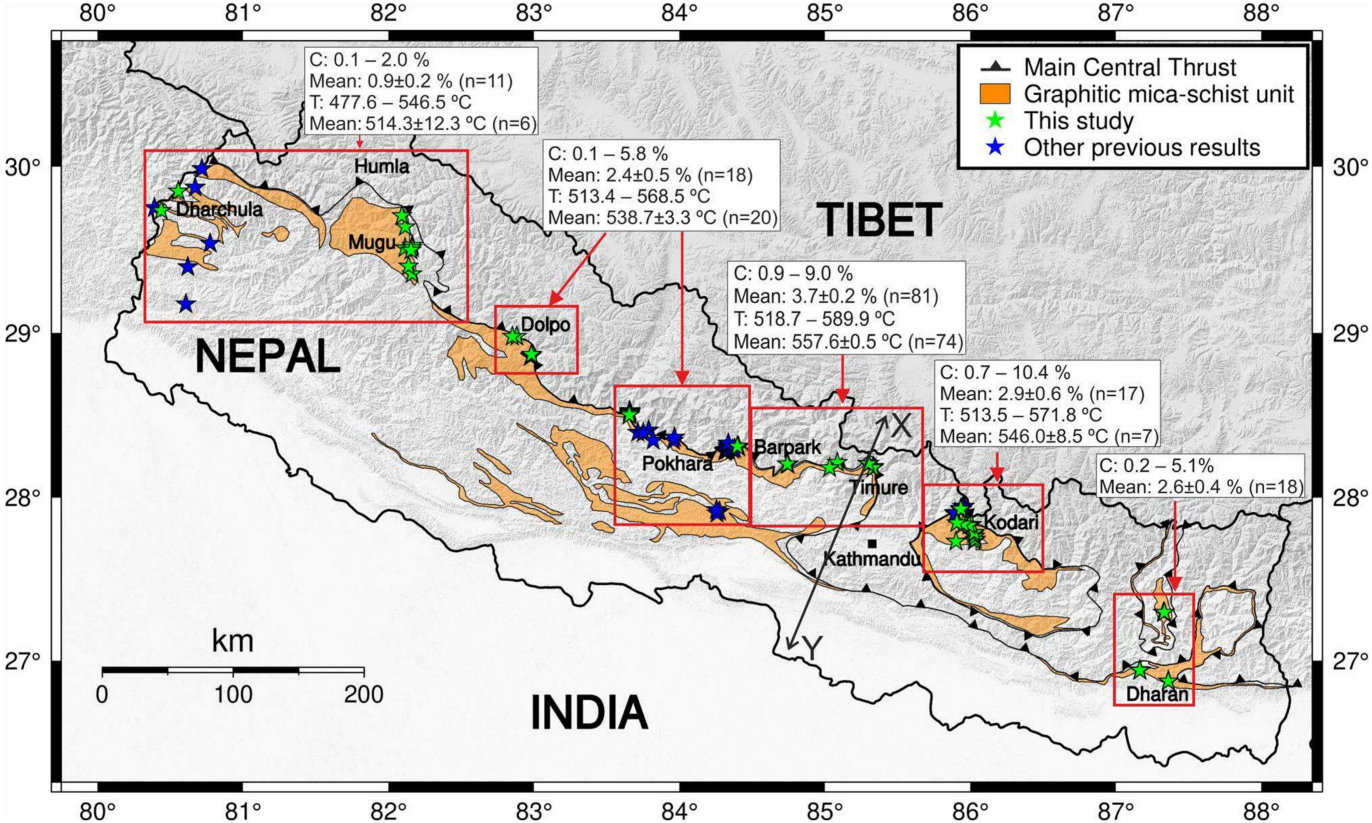
80°
81°
82°
83°
84°
85°
86°
87°
88°
30°
29°
28°
27°
Main Central Thrust
Graphitic mica-schist unit
This study
Other previous results
C: 0.1 – 2.0 %
Mean: 0.9±0.2 % (n=11)
T: 477.6 – 546.5 °C
Mean: 514.3±12.3 °C (n=6)
C: 0.1 – 5.8 %
Mean: 2.4±0.5 % (n=18)
T: 513.4 – 568.5 °C
Mean: 538.7±3.3 °C (n=20)
C: 0.9 – 9.0 %
Mean: 3.7±0.2 % (n=81)
T: 518.7 – 589.9 °C
Mean: 557.6±0.5 °C (n=74)
C: 0.7 – 10.4 %
Mean: 2.9±0.6 % (n=17)
T: 513.5 – 571.8 °C
Mean: 546.0±8.5 °C (n=7)
C: 0.2 – 5.1%
Mean: 2.6±0.4 % (n=18)
Humla
Dharchula
Mugu
Dolpo
TIBET
NEPAL
Pokhara
Barpark
Tinure
Kodari
Kathmandu
Dharan
X
Y
km
0
100
200
INDIA

Figure 15

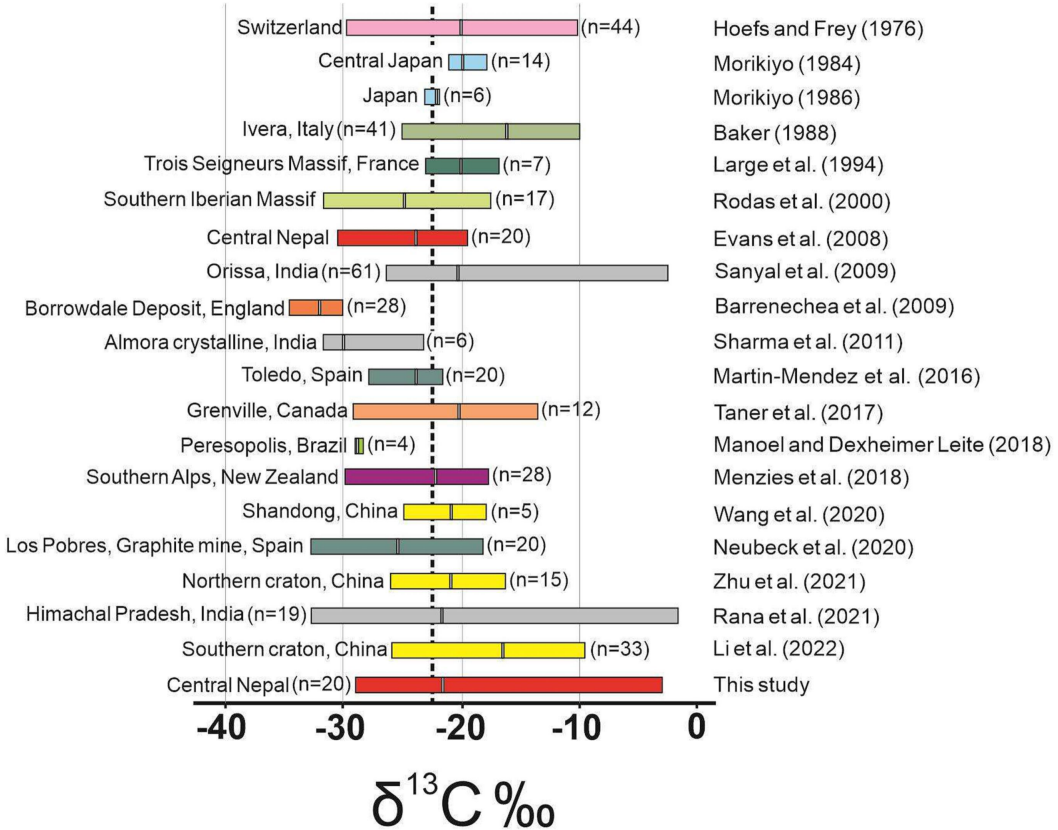
Switzerland (n=44) Hoefs and Frey (1976)
Central Japan (n=14) Morikiyo (1984)
Japan (n=6) Morikiyo (1986)
Ivera, Italy (n=41) Baker (1988)
Trois Seigneurs Massif, France (n=7) Large et al. (1994)
Southern Iberian Massif (n=17) Rodas et al. (2000)
Central Nepal (n=20) Evans et al. (2008)
Orissa, India (n=61) Sanyal et al. (2009)
Borrowdale Deposit, England (n=28) Barrenechea et al. (2009)
Almora crystalline, India (n=6) Sharma et al. (2011)
Toledo, Spain (n=20) Martin-Mendez et al. (2016)
Grenville, Canada (n=12) Taner et al. (2017)
Peresopolis, Brazil (n=4) Manoel and Dexheimer Leite (2018)
Southern Alps, New Zealand (n=28) Menzies et al. (2018)
Shandong, China (n=5) Wang et al. (2020)
Los Pobres, Graphite mine, Spain (n=20) Neubeck et al. (2020)
Northern craton, China (n=15) Zhu et al. (2021)
Himachal Pradesh, India (n=19) Rana et al. (2021)
Southern craton, China (n=33) Li et al. (2022)
Central Nepal (n=20) This study
-40
-30
-20
-10
0
δ13C ‰

Figure 16

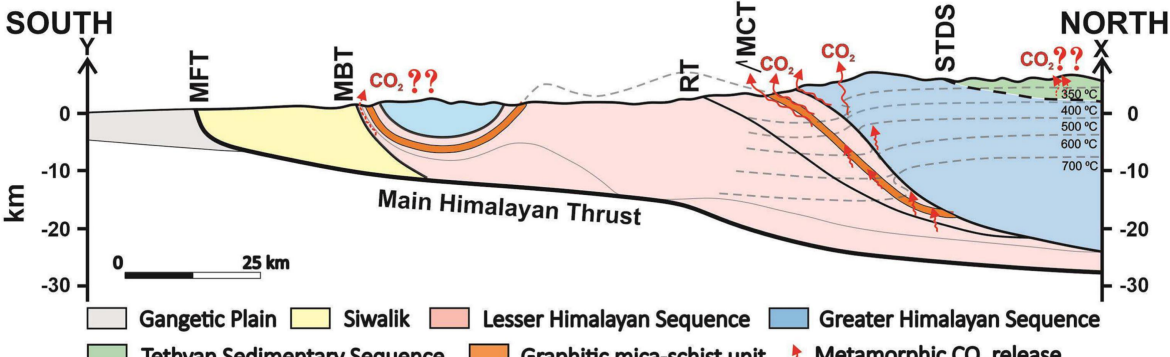
SOUTH
NORTH
Y
X
MFT
MBT
MCT
RT
STDS
CO_2 ??
CO_2
CO_2
CO_2??
350 °C
400 °C
500 °C
600 °C
700 °C
km
0
-10
-20
-30
Main Himalayan Thrust
0
25 km
Gangetic Plain
Siwalik
Lesser Himalayan Sequence
Greater Himalayan Sequence
Tethyan Sedimentary Sequence
Graphitic mica-schist unit
Metamorphic CO_2 release

Figure 17